



HAL
open science

Separatrix parameters and core performances across WEST L-mode database

Clarisse Bourdelle, Jorge Morales, Jean-François Artaud, Tennessee Radenac,
Jérôme Bucalossi, Guido Ciraolo, Frédéric Clairet, Rémi Dumont, Nicolas
Fedorczak, Christophe Gil, et al.

► **To cite this version:**

Clarisse Bourdelle, Jorge Morales, Jean-François Artaud, Tennessee Radenac, Jérôme Bucalossi, et al.. Separatrix parameters and core performances across WEST L-mode database. Nuclear Fusion, 2023, 63 (5), pp.056021. 10.1088/1741-4326/acbf . cea-04062711

HAL Id: cea-04062711

<https://cea.hal.science/cea-04062711>

Submitted on 7 Apr 2023

HAL is a multi-disciplinary open access archive for the deposit and dissemination of scientific research documents, whether they are published or not. The documents may come from teaching and research institutions in France or abroad, or from public or private research centers.

L'archive ouverte pluridisciplinaire **HAL**, est destinée au dépôt et à la diffusion de documents scientifiques de niveau recherche, publiés ou non, émanant des établissements d'enseignement et de recherche français ou étrangers, des laboratoires publics ou privés.



Distributed under a Creative Commons Attribution 4.0 International License

Separatrix parameters and core performances across the WEST L-mode database

C. Bourdelle^{*}, J. Morales, J.F. Artaud, O. Grover¹, T. Radenac, J. Bucalossi, Y. Camenen², G. Ciralo, F. Clairet, R. Dumont, N. Fedorczak, J. Gaspar³, C. Gil, M. Goniche, C. Guillemaut, J. Gunn, P. Maget, P. Manas, V. Ostuni, B. Pégourié, Y. Peysson, P. Tamain, L. Vermare, D. Vézinet and the WEST Team^a

CEA, IRFM, F-13108 Saint-Paul-lez-Durance, France

¹ Max-Planck-Institute for Plasma Physics, Boltzmannstr. 2, D-85748 Garching, Germany

² CNRS, Aix-Marseille University, PIIM, UMR7345 Marseille, France

³ Aix Marseille University, CNRS, IUSTI, Marseille, France

E-mail: clarisse.bourdelle@cea.fr

Received 23 September 2022, revised 20 February 2023

Accepted for publication 28 February 2023

Published 5 April 2023



CrossMark

Abstract

WEST database analysis shows a correlation of the recycled neutral source around the separatrix with core performances. This observation questions the causality chain between particle source and turbulent transport up to the core in L-mode, high recycling plasmas, an unavoidable phase of all scenarios. The best core performances correlate with the lowest values of the density at the separatrix, n_{sep} , similarly to ASDEX Upgrade (AUG) tokamak and Joint European Torus (JET) tokamak in H-mode (Verdoolaege *et al* 2021 *Nucl. Fusion* **61** 076006). Reflectometry in the midplane provides n_{sep} , while the temperature at the separatrix, T_{sep} is inferred by the ‘two-point model’ using Langmuir probe data on divertor targets. Lower separatrix resistivity does not correlate with better core performances, unlike H-mode observations (Eich *et al* 2020 *Nucl. Fusion* **60** 056016). As expected in the presence of an efficient neutral source due to recycling fluxes, n_{sep} correlates with the D recycled particle flux at the divertor measured by visible spectroscopy. Coherently, at a given controlled central line integrated density \bar{n} , lower n_{sep} correlates with a larger density gradient around the separatrix as well as a larger global density peaking, $\bar{n}/\langle n \rangle$, measured by interferometry. The latter correlates as well with lower collisionality in the core, similarly to JET and AUG H-modes (Angioni *et al* 2007 *Nucl. Fusion* **47** 1326). The correlations reported allow phrasing the subsequent causality question: what is the interplay chain between low neutral recycling at the divertor plates, low density at the separatrix, high density peaking at the separatrix, high global density peaking, higher central temperature and better core energy confinement quality? Understanding the causality chain is essential to prepare ITER operation and design DEMO scenarios where the ratio of the divertor leg to the ionization length will be larger and where the pumped flux with respect to the plasma volume will be lower than presently operating tokamaks.

^a see <http://west.cea.fr/WESTteam>.

^{*} Author to whom any correspondence should be addressed.



Original content from this work may be used under the terms of the [Creative Commons Attribution 4.0 licence](https://creativecommons.org/licenses/by/4.0/). Any further distribution of this work must maintain attribution to the author(s) and the title of the work, journal citation and DOI.

Keywords: plasma, tokamak, database, confinement, separatrix

(Some figures may appear in colour only in the online journal)

1. Introduction

WEST is a full W environment tokamak (main chamber including antenna limiters and baffle, as well as both upper and lower divertors). It operates at 3.7 T, up to 1 MA, with a plasma volume of 15 m³ and an aspect ratio between 5 and 6. Continuous wave RF power is installed: up to 9 MW of ion cyclotron resonant heating (ICRH) power and 7 MW of low hybrid current drive (LHCD).

During its first phase of operation, up to 9.2 MW of combined ICRH and LHCD power has been reached and pulses lasting up to 55 s have been routinely achieved [1]. In L-mode, the stored energy, W_{MHD} , increases according to the ITER96 L-mode scaling law confirming its weak aspect ratio dependence [2]. Some L–H transitions have been observed [3] for a power crossing the separatrix of the order of the ‘Martin 2008’ scaling law [4].

WEST experimental data is natively in the Integrated and Modelling Analysis Suite (IMAS) format [5]. The data treatment chain provides systematic temperature and density fitted profiles from the core to the separatrix, the magnetic equilibrium is rerun between pulses including polarimetry constrains and the Langmuir probes data treatment is automated, etc. This approach allows automatic production of a very large L-mode database accessible to the whole WEST team. The database of 1249 D pulses resulting from two campaigns is exhaustively analyzed here.

In WEST L-mode high recycling plasmas, two regimes of operation are encountered [6]. Either the central electron temperature, $T_e(0)$, increases with larger ratio of the total power to the volume averaged density, $P_{\text{tot}}/\langle n \rangle$, or it remains frozen below ≈ 2 keV. The extensive and exhaustive database analysis allows us to show that the so-called ‘cold branch’ is associated with larger density at the separatrix, n_{sep} .

Such results echo recent H-mode database studies on both Joint European Torus (JET) [7–9]⁴ and ASDEX Upgrade (AUG) tokamak [10–13] where larger n_{sep} are associated with degraded plasma core performances. The density at the separatrix is determined by the interplay between transport, MHD and source (ionization of neutrals) [14].

In H-mode, higher pressure in the separatrix area leads to a critical ideal MHD limit encountered at larger normalized radius, leading to lower pressure at the pedestal top and hence lower global confinement [12]. In some of the JET H-modes, with a pedestal pressure below the ideal limit, the resistive modes onset might play a role [8]. The key role of the collisionality at the separatrix, driving resistive modes, was proposed in AUG H-mode database analysis [11]. And actually it traces back from the late 1990s, when Scott [15–17] and Rogers *et al* [18] fluid models were compared to experimental

scrape-off layer plasma (SOL) data in L- and H-modes, see for example [19]. It actively continues today by comparing experimental trends to state-of-the-art edge simulations using gyrokinetic codes [20–23] and fluid nonlinear simulations [24–30]. Following the path of Scott and Rogers–Drake–Zeiler, fluid-based turbulent models are capturing qualitatively and quantitatively the density limit and/or the L–H transition [27, 28, 30, 31].

Concerning the role of neutral penetration, earlier studies stipulated that it strongly influenced separatrix parameters such as density and temperature. For example, a multi-machine International Tokamak Physics Activity (ITPA) work showed that T_{sep} is sensitive to details of the neutral recycling process [14]. And indeed, the widely used pedestal fit based on a modified hyperbolic tangent is inferred from a neutral penetration model [32–34]. Neutrals are also thought to play a role in density shoulder formation in the SOL, see [35] and older references therein. Concerning the impact on temperature, thanks to turbulence gyrokinetic simulations using XGC1, the charge-exchange by neutrals has been shown to steepen the ion temperature profile, hence enhancing the drive for ion temperature gradient modes [36]. Additionally, removing neutrals, thanks to a pumping lithium environment in the Lithium Tokamak Experiment (LTX), has been demonstrated experimentally to produce a flat temperature with a hot separatrix temperature [37].

Disentangling the role of neutrals, turbulence and MHD on separatrix, pedestal and core parameters remains an open issue. A way of addressing this challenge is to perform exhaustive experimental database analysis, where correlations between SOL, separatrix and core parameters are extensively explored.

Indeed, it is crucial to understand the potential impact of separatrix conditions on core confinement in both L and H-modes in today’s tokamaks in order to extrapolate towards ITER and DEMO, where simultaneous high core confinement and large n_{sep} are expected. ITER scenarios are projected to reach $H_{98y,2} = 1$ [38] while DEMO design is aiming at $H_{98y,2} = 1.1$ – 1.4 [39]. High density at the separatrix is required for multiple reasons in these foreseen high recycling W environments: to reduce the W sputtering by reducing the divertor target temperature and to maximize the pressure in the vicinity of the pumps. As a side effect, large recycling regimes might also be beneficial to maximize the tritium global recycling coefficient at the separatrix and hence its burn up [40].

Extrapolating empirically today’s observation towards ITER or DEMO is not possible. Indeed, only for the role of neutrals in the pedestal-forming region, the conditions in ITER and DEMO are anticipated to be very different due to (a) larger divertor legs and wall clearance with respect to the ionization length [41] and (b) a lower pumping/fueling versus plasma volume: for example DEMO pumping efficiency is foreseen to be 8 times larger than AUG’s, while DEMO plasma volume

⁴ Note that in the JET metal wall the strong impact of higher triangularity, δ , allowing to reach Greenwald density for $H_{98y,2} = 1$ [86] was not recovered.

is foreseen to be more than 100 times larger than AUG's [42]. It is therefore mandatory to take advantage of the great variety in today's tokamaks in terms of pumping/fueling⁵, divertor geometry⁶ and divertor material⁷ to challenge our ability to predict the density at the separatrix and its correlation with core performances.

Studying L-modes, which have a similar correlation as H-modes, namely a lower confinement with larger n_{sep} , will help disentangle the role of turbulent transport versus neutral particle source, while avoiding the additional interplay with pedestal stability/transport. Moreover, L-mode plasmas are of interest as these phases are first encountered when characterizing a new machine's operational domain and the L-mode pedestal-forming region physics is likely key to understanding H-mode access [43].

L-mode interplay between neutral penetration and turbulent transport remains a topic to be further explored. At present, gas puff modulations on AUG show that larger n_{sep} is associated with poorer $T_e(0)$ and even a cold pulse. Resistive modes could be at play to explain the enhanced heat transport [44]. On JET, particle transport in a normalized collisionality scan has been modeled, but not for a normalized minor radius, ρ , larger than 0.8 [45]. On TEXTOR tokamak (TEXTOR), during the radiative improved mode investigation, the density profile steepening just inside the separatrix was hypothesized as a key stabilizing parameter of Ion Temperature Gradient (ITG) allowing H-mode-like core performances in an L-mode plasma [46, 47].

In this context, we are exploring the WEST L-mode database. Similarly to what is foreseen in ITER, electron heating dominates (ICRH and LHCD-heated plasmas) and there is no central particle or torque source (no Neutral Beam Injection (NBI)). The counterpart of ICRH and LHCD heating is that it is important to disentangle the impact of n_{sep} on the core confinement from its impact on modified coupling and hence modified core heating sources.

In the present paper, we analyze exhaustively two campaigns of WEST phase 1 (prior to the completion of the actively cooled ITER-like lower divertor): C4 and C5. It is a D plasma database, in L-mode at 3.7 T. By manipulating a large database of more than 1200 pulses, we explore exhaustively the operational domain of the machine, avoiding as much as possible bias induced by a cherry-picking approach. Data averaged on more than 3600 plateaus are collected.

In section 2, the database building is explained, while in section 3 the co-existence of a cold and a hot branch for a given ratio of the total power to the volume averaged density is presented. In section 4, the correlation between density (line average, at the separatrix, global peaking) and core confinement is presented. The possible role of modified turbulence around the separatrix is reported in section 5 where

the correlation between the separatrix collisionality and global confinement is described. Finally, in section 6, the role of neutral fueling/recycling on n_{sep} and the density gradient is presented. The results are summarized and discussed in the last section, section 7.

2 Database building

All WEST experimental data are natively archived in IMAS data structures such as core_profile, equilibrium, etc [5]. The data treatment chain runs systematically on each pulse, from breakdown to termination. The philosophy is to automate as many data treatments as possible and make them available to all in a systematic manner. For example, automated fits of the temperature and density profiles are provided for each pulse every 10 ms. The treated Langmuir probes data (parallel heat fluxes, density and temperature along the divertor targets) are systematically and automatically generated, a polarimetry-constrained equilibrium is performed between pulses using NICE [48, 49], etc.

Moreover, there is an IMAS data structure named 'summary' which is used to store 0D quantities. These quantities are time averaged over plateaus of total power intersecting plasma current plateaus whose duration exceeds 0.3 s.

The database contains time-averaged quantities over 3685 plateaus coming from 1249 D pulses. They exhaustively cover the C4 and C5 campaigns, at the exclusion of the He part of the C4 campaign [50]. The pulses are mostly ohmic- or RF-heated L-mode plasmas, and eight pulses have transitions in H-mode [3]. All the plateaus are at 3.7 T with the plasma current, I_p , in the range 0.2–0.8 MA, the auxiliary power, P_{AUX} , varying from 0.5 to 9 MW and the electron volume averaged density, n_e , between 1 and 9 $\times 10^{19} \text{ m}^{-3}$. Of these plateaus, 43% have a total absorbed power above 1 MW and 60% of these externally heated plateaus have more than 80% of the RF power from LHCD.

Eight hundred plateaus with characteristics of total power (P_{tot}) above 2 MW, plasma current 0.5 MA, in lower single null (LSN), and using D₂ gas puff only (excluding four pellet-fueled plasmas) are the main focus of the database analysis presented in the following. Note that 88% of the plateaus at $P_{\text{tot}} > 2 \text{ MW}$ are at 0.5 MA. We therefore limit our analysis to this unique plasma current. By choosing $P_{\text{tot}} > 2 \text{ MW}$, we exclude all ohmic phases (the ohmic power varies between 0.3 and 0.8 MW for $I_p = 0.5 \text{ MA}$) and focus on L-mode plateaus only. Eighty-eight percent of the LSN L-mode plateaus are at 0.5 MA; we therefore select plateaus at 0.5 MA only to ease our scaling law discussion. The LSN pulses are chosen as the connection of the Langmuir probes acquisition system was optimized for this magnetic configuration during the C4 and C5 campaigns, moreover, in the database more than 9 plateaus out of 10 are in LSN. Table 1 illustrates the range of parameters of this sub-database. Moreover, histograms of this sub-database, figure 1, show that: (1a) LHCD is the dominant heating; (1b) P_{tot} averaged over the plateau time duration

or lithium-based coatings.

⁵ e.g. a few $\text{Pa}\cdot\text{m}^3\text{s}^{-1}$ on WEST turbomolecular pumps and up to

⁶ $50 \text{ Pa}\cdot\text{m}^3\text{s}^{-1}$ on AUG cryopumps for a similar plasma volume of 15 m^3 .

⁷ e.g. vertical versus horizontal targets on JET, closed AUG divertor versus

open DIII-D or WEST divertors, etc.

⁸ e.g. C divertors in DIII-D, W divertors in AUG, JET, WEST as well as boron-

reaches up to 8 MW with a mean value over the database of 8.6 MW, (3) the Greenwald fraction ranges mostly between 40% and 60% around a mean value of 50%; (1d) radiated

Table 1. Range of plateau-averaged quantities of some of the key parameters of the C4 and C5 database such that: $I_p = 0.5$ MA, D plasmas only, Lower Single Null (LSN), $P_{tot} > 2$ MW. The parameters are the geometrical major radius R_{geo} , the minor radius a , the toroidal magnetic field B_T , the elongation κ , the triangularity δ , the line average density \bar{n} , the LHCD power P_{LHCD} , the ICRH power P_{ICRH} and finally P_{tot} the total power (ohmic and auxiliary).

main ion	R_{geo} (m)	a (m)	B_T (T)	I_p (MA)	κ	δ	\bar{n} ($10^{19}m^{-3}$)	P_{LHCD} (MW)	P_{ICRH} (MW)	P_{tot} (MW)
D	2.33–2.59	0.39–0.47	3.67–3.78	0.48–0.55	1.29–1.58	0.38–0.55	2.51–6.20	0–5.31	0–3.15	2.00–8.01

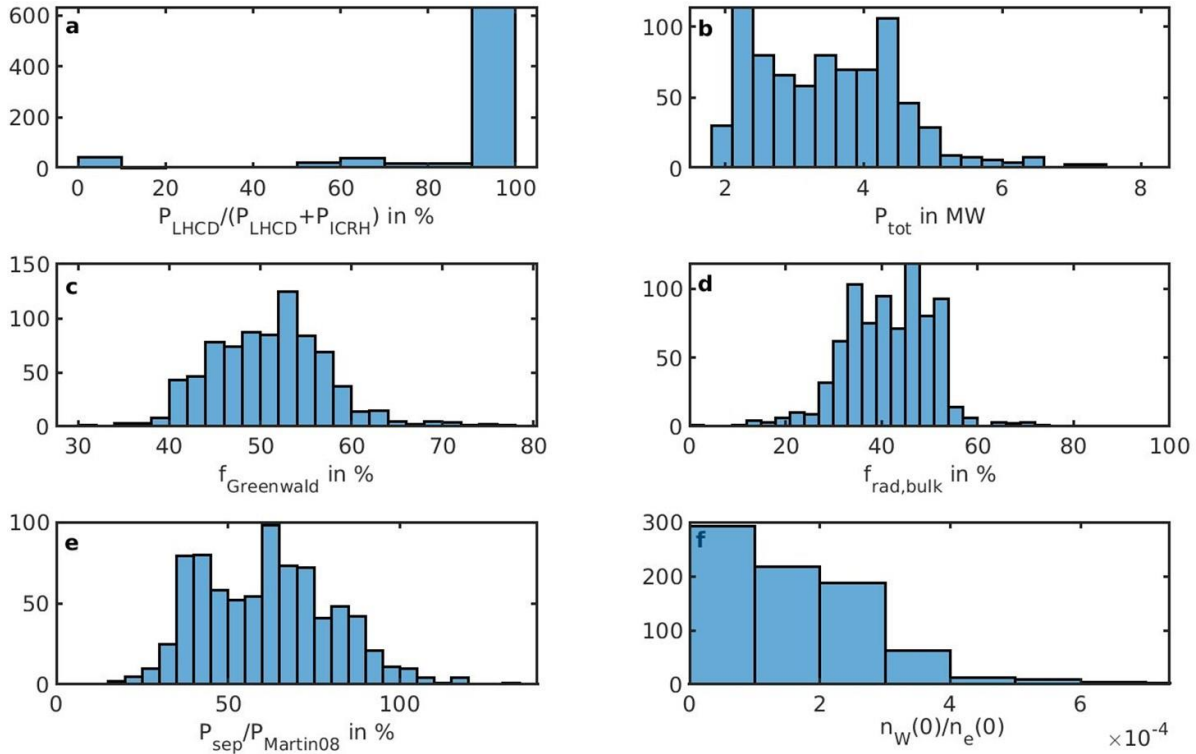


Figure 1. Histograms of the 800 plateaus from the C4 and C5 database such that: $I_p = 0.5$ MA, D plasmas only, LSN, $P_{tot} > 2$ MW. In (c), $f_{Greenwald}$ is the Greenwald fraction: $\bar{n}/(I_p/\pi a^2)$. In (d), $f_{rad,bulk} = P_{rad,bulk}/P_{tot}$ is the fraction of the radiative power in the plasma bulk, inside the separatrix, $P_{rad,bulk}$, to the total power P_{tot} . In (e), P_{sep} is the power crossing the separatrix, i.e. $P_{sep} = P_{tot} - P_{rad,bulk}$ with the radiative power in the plasma bulk, inside the separatrix. P_{sep} is normalized to the power threshold to enter in H mode predicted by the ‘Martin scaling law’ [4], $P_{Martin08}$. $f_{rad,bulk} = P_{rad,bulk}/P_{tot}$. In (f), the W concentration in the core with respect to the electron density is plotted: $n_W(0)/n_e(0)$.

power in the confined plasma is on average 42% of the total power; (1e) the power crossing the separatrix is above the Martin scaling law [4] only for 24 plateaus but actually only 5 plateaus are effectively in H-mode in LSN, see [3] for more details on the H-mode phases; (1f) the core W concentration, $n_W(0)/n_e(0)$, ranges from 3×10^{-5} to 7×10^{-4} , with a mean value of 2×10^{-4} .

In the following, various sub-ensembles of this database will be studied. For example, when the density at the separatrix by reflectometry is required, the data set is restricted to the pulses in which reflectometry reconstructed profiles are available (603 plateaus out of 800). The smallest sub-ensemble of plateaus used in the work presented here is made of 595 plateaus.

3. Coexistence of a cold branch with a hot one in the WEST database

There is an operational domain for WEST L-mode dominantly heated by LHCD. This operational domain is such that, at a

given power, if the density is too low, the power is not coupled (the empty triangle at low density, high power in the figure 2), and if the density is too large, the electron temperature remains below 2 keV (the blue points in figure 2). This T_e clamping is due to the presence of W. Indeed below 2 keV, a vicious circle takes place where the W cooling factor increases with lower temperature, leading to hollow T_e profiles and MHD instability. Therefore there is a narrow range of $(P_{tot}, \langle n \rangle)$ over which T_e in the core reaches more than 2 keV, in red in figure 2.

By plotting the central electron temperature, $T_e(0)$, against the ratio of the total power divided by the volume-averaged density, we observed the existence of two branches [2] at $I_p = 0.5$ MA, $B_T = 3.7$ T. The ‘hot branch’ exhibits a $T_e(0)$ which increases with increasing ratio of the total power to the volume-averaged density, $P_{tot}/\langle n \rangle$, and a ‘cold branch’ where $T_e(0)$ does not increase with larger $P_{tot}/\langle n \rangle$ and remains below 2 keV, as illustrated in figure 3(a).

As expected, the hot branch is characterized by a higher energy content, see figure 3(b). Additionally, the measured DD

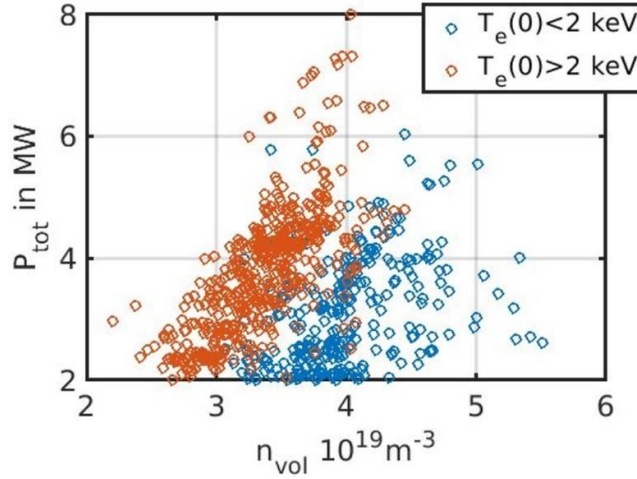


Figure 2. WEST C4 and C5 L-mode database, $B = 3.7$ T, $I_p = 0.5$ MA, LSN, D only, $P_{tot} > 2$ MW. Time-averaged total power, P_{tot} , over the plateaus plotted against the volume-averaged electron density, n_{vol} in figure legend and $\langle n \rangle$ in the text. In red time-averaged $T_e(0)$ over the plateaus above 2 keV and in blue below 2 keV.

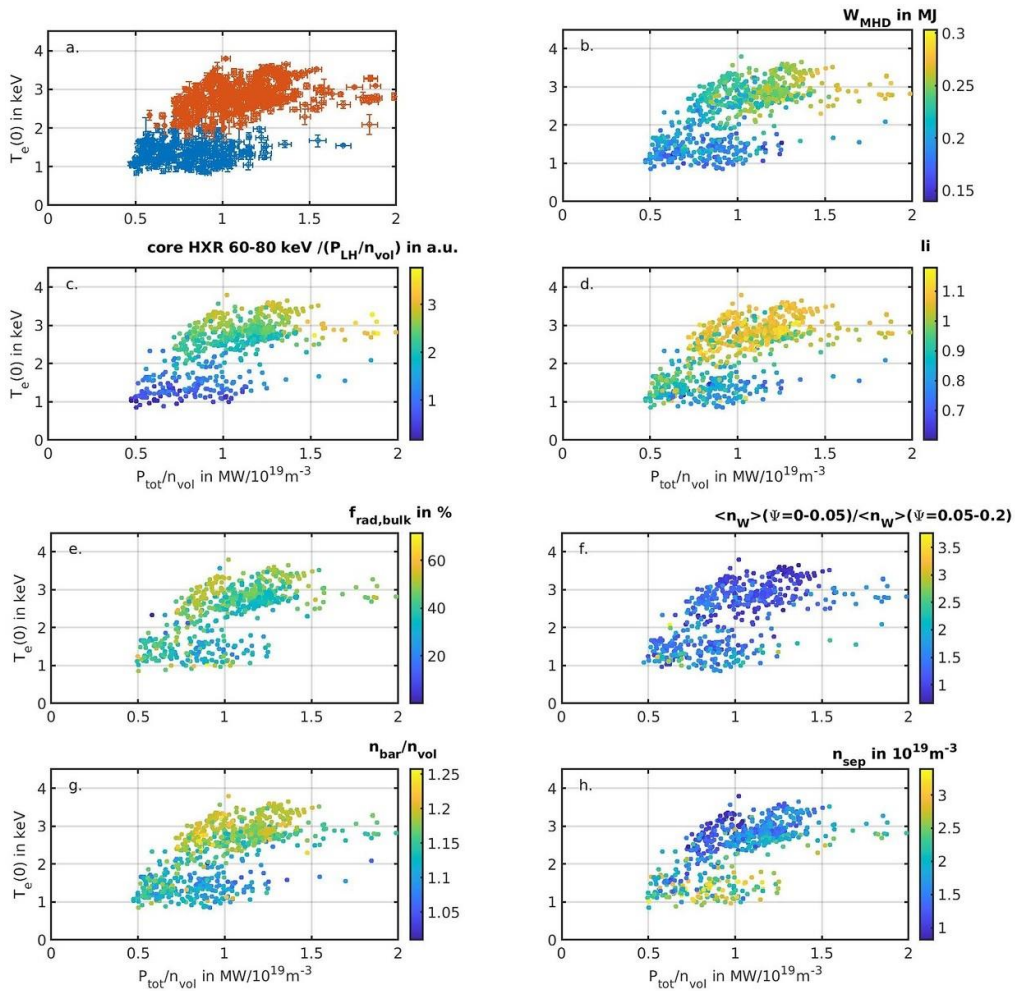


Figure 3. WEST C4 and C5 L-mode database, $B = 3.7$ T, $I_p = 0.5$ MA, LSN, D only, $P_{tot} > 2$ MW. In this series of plots, $T_e(0)$ is plotted against the ratio P_{tot}/n_{vol} . All the quantities are time averaged over the plateaus. In (a) the error bars on $T_e(0)$ are from the standard deviation obtained on the plateaus over which $T_e(0)$ is time averaged. For figures (b) to (h), the colour code corresponds to a physics quantity: (b) the plasma energy content produced by the MHD equilibrium code NICE, W_{MHD} ; (c) the core Hard X Ray signal in the energy range from 60 to 80 keV normalized to the ratio of P_{LHCD}/n_{vol} ; (d) the internal inductance, li , from the MHD equilibrium code NICE; (e) $f_{rad,bulk} = P_{rad,bulk}/P_{tot}$ the radiative power in the plasma bulk; (f) the core W density peaking represented by the ratio of W density at normalized poloidal flux, Ψ , between 0 to 0.05 normalized to the W density slightly more outward, at normalized poloidal flux 0.05-0.2; (g) density peaking given by the ratio between the line averaged density n_{bar} to the volume averaged density n_{vol} ; (h) the density at the separatrix, n_{sep} , obtained by reflectometry (the database is reduced to the plateaus on which the reflectometry was available) and using the magnetic equilibrium reconstruction by NICE constrained by polarimetry angles.

neutron rate is higher on the hot branch (not shown here) as a signature of hotter ions as well as hotter electrons.

Our database is predominantly LHCD heated (see figure 1). The LHCD absorption signature on the inversed of hard x-ray signal peaks inside $\rho = 0.3$ (for 83% of the 678 plateaus on which the hard x-ray diagnostic is available). Due to central LHCD, the majority of the plasmas analyzed here are sawtooth-free. Since LHCD absorption is more central in hotter plasmas [51], we cannot disentangle precisely the causality between more central LH heating and larger $T_e(0)$. This strong correlation is illustrated in figure 3(c), where core fast electrons due to LHCD absorption are diagnosed by hard x-ray signal along the central horizontal chord normalized to $P_{\text{LHCD}}/(\bar{n} \langle n \rangle)$ in the 60–80 keV range [52].

As expected, the current profiles are more peaked on the hot branch due to more centrally absorbed LHCD and lower resistivity, leading to higher internal inductance (figure 3(d)).

In terms of fraction of radiative power, there is no clear distinction between the hot and the cold branches as illustrated by figure 3(e). The fraction of radiated power in the confined plasma measured by bolometry [53] is around 42% (figure 1), independent of the RF power level or whether operating LHCD or ICRH [1, 2, 54].

Regarding the W profile in the core, over the whole database the core W concentration, $n_w(0)/n_e(0)$, ranges from 3×10^{-5} to 7×10^{-4} , with a mean value of 2×10^{-4} (see figure 1). The core W peaking is similar and rather flat on both branches as illustrated in figure 3(f). The W content, in the full W environment of WEST, is obtained assuming that for $T_e(0) > 1$ keV, the radiated power measured by bolometry is only due to W radiation—more details are given in [6].

Concerning the electron density profiles, interestingly, the global density peaking parameter is larger on the hot branch. This peaking factor is based on eight interferometry line-averaged density chords [55] inverted to produce the line-averaged and volume-averaged densities, respectively \bar{n} (\overline{ornbar}) and $\langle n \rangle$ ($\langle ornvol \rangle$), the ratio of which is a proxy for the global density profile peaking: $\bar{n}/\langle n \rangle$. Finally, lower n_{sep} is observed on the hot branch with respect to the cold branch, figure 3(h). The density at the separatrix is measured by reflectometry in the outboard midplane [56], remapped on the magnetic equilibrium reconstructed by NICE constrained by eight polarimetry Faraday angles [55].

In the following, we set a pragmatic criterion to define the hot branch: $T_e(0) > 2$ keV. Sixty-four percent of the plateaus are on the hot branch. The time traces of the pulses entering the hot or cold branches are illustrated in [6]. Thanks to the database analysis, we have found an operational minimum ratio of P_{LHCD}/\bar{n} necessary to avoid the cold branch and above which we will systematically operate in the future [57]. We have also understood the mechanisms leading to the collapse of 1/4th of the pulses from the hot to the cold branch thanks to an integrated modeling of two collapsing plasmas [6]. The LHCD absorption moving more off axis as the temperature drops, combined with a more centrally peaked W density due to reduced neoclassical temperature screening, have been identified as key players. The trigger leading to the initial temperature dropping remains to be identified.

The importance of density control is likely key, as we observe lower density at the separatrix on the hot branch (note that no correlation between n_{sep} and LHCD coupling is found in the database, see appendix A).

In the following section, the impact of density in various forms: \bar{n} , n_{sep} and $\bar{n}/\langle n \rangle$ on the overall confinement time is explored on the whole database, including the cold and hot branches, i.e. plateaus on which the time-averaged $T_e(0)$ is lower or higher, respectively, than 2 keV.

4. Density impact on energy confinement time

In this section, we will review the density impact on the energy confinement time through three quantities:

- The line-averaged density, \bar{n} , traditionally used in global multi-machine scaling laws.
- The density at the separatrix, n_{sep} , shown to anticorrelate with normalized confinement time in JET and AUG H-modes [10, 13] and to be lower on the hot branch in WEST L-mode, figure 3(h).
- The global density peaking, $\bar{n}/\langle n \rangle$, found to be higher on the hot branch, see figure 3(g).

4.1. Impact of the line-averaged density on the confinement time

In both the L-mode and H-mode reference scaling laws for ITER, L₉₆ and H_{98y,2}, the confinement increases with higher line-averaged density values [58, 59], respectively: $\tau_E^{96L} \propto \bar{n}^{0.24}$ and $\tau_E^{98ELMy} \propto \bar{n}^{0.44}$. Such scalings have been revised following the metallic devices (JET and AUG) results [9] and the new ITPA 2020 scaling law [13] for ELMy H-mode reports a weaker trend with respect to density: $\tau_E^{\text{ITPA20-IL}} \propto \bar{n}^{0.147 \pm 0.097}$.

The WEST L-mode database has been added to the existing ITER L-mode databases used to derive the ITER89-P [60] and ITER96-L scaling laws [58]. This exercise is presented in detail in chapter 3 of Ostuni's PhD [61] as well as more succinctly in [2].

The confinement time is defined using W_{MHD} , the energy content given by the MHD equilibrium calculation constrained by polarimetry by NICE [48, 49]. W_{MHD} is favored instead of W_{th} , the thermal energy content, due to the absence of systematic temperature profile measurements during the first phase of WEST operation (the electron temperature is measured by Electron Cyclotron Emission (ECE), hence, in the presence of LHCD fast electrons, data is available up to mid-radius and the ion temperature measured by a 2D X spectrometer was not systematically available). The suprathreshold electron contribution to the total energy content is expected to be below 5% [62] in the present database, where 90% of the total RF power above 2 MW is from LHCD (see figure 1). Hence, under such conditions W_{MHD} is expected to be a good approximation for W_{th} .

The WEST L-mode database of more than 1000 entries (W_{MHD}) is added to the ITER96-L W_{th} database of 1312 entries coming from 12 different tokamaks. In the ITER96-L database the radiated power has not been subtracted from the

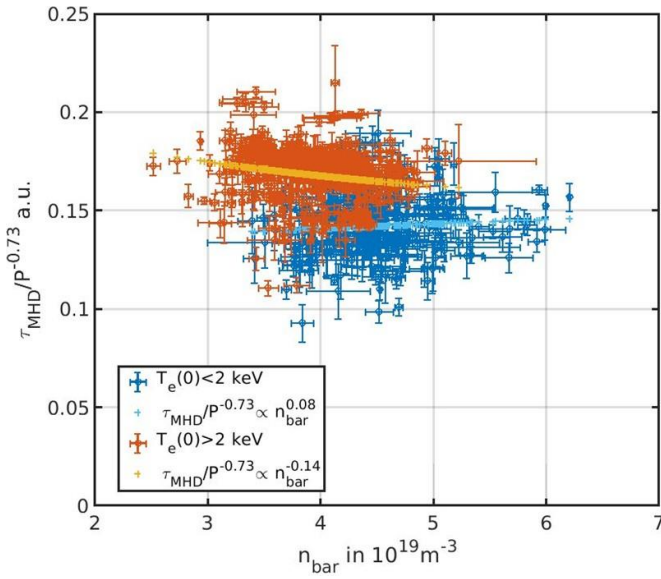


Figure 4. WEST C4–C5 L-mode database, $B = 3.7$ T, $I_p = 0.5$ MA, D only, LSN, $P_{tot} > 2$ MW. The error bars represent the standard deviation measured during the plateaus over which the quantities are time averaged. The confinement time is normalized to the power dependence of the WEST scaling law [2, 61]: $P^{-0.73}$.

total power. For WEST, the radiated power in the bulk is, on average, 42% of the total power (see figure 1). Therefore, the impact on the scaling law of subtracting $P_{rad,bulk}$ from P_{tot} is explored and shown to weakly affect the scaling law coefficients, in particular the power degradation exponent changes from $P_{tot}^{-0.73}$ to $(P_{tot} - P_{rad,bulk})^{-0.76}$, see appendix 1 of [2] and chapter 3 of [61]. The weak aspect ratio dependence of the ITER96-L scaling law is confirmed [2]. A linear regression on WEST-only data reduces the rms down to 12.7%, the main difference with ITER96-L is a strongly reduced impact of \bar{n} , while the power degradation remains identical to ITER96-L, namely scaling as $P^{-0.73}$, see table 1 of [2].

Based on the work on WEST scaling laws published in [2, 61], in our reduced D L-mode database in LSN, at $I_p = 0.5$ MA and $P_{tot} > 2$ MW, the confinement time, τ_{MHD} , is estimated using W_{MHD} normalized to P_{tot} , the total power. The database being at a unique I_p , τ_{MHD} is normalized only to the power degradation reported for WEST: $P^{-0.73}$ [2, 61] with $P = P_{tot}$.

The impact of the line-averaged density, \bar{n} , traditionally used in global multi-machine scaling laws, is explored in this reduced database, before exploring other forms of the density. In figure 4, on the cold branch, where $T_e(0) < 2$ keV, the confinement time is mostly insensitive to \bar{n} : $\tau_{MHD}/P^{-0.73} \propto \bar{n}^{0.08}$ while on the hot branch, for $T_e(0) > 2$ keV, it even degrades with larger density: $\tau_{MHD}/P^{-0.73} \propto \bar{n}^{-0.14}$.

4.2 Impact of the density at the separatrix on the confinement time

Concerning the impact of the density at the separatrix, similarly to H-mode databases [9, 10, 13], in our L-mode database, a degradation of the confinement with higher n_{sep} is reported. Note that the Greenwald density, at 0.5 MA, ranges between

7 and $10 \times 10^{19} m^{-3}$, hence, n_{sep} normalized to the Greenwald density is below 50%.

The density at the separatrix is measured by reflectometry in the outboard midplane [56], remapped on the magnetic equilibrium reconstructed by NICE constrained by eight polarimetry Faraday angles [48, 49] and averaged over the plateaus. In figure 5, the confinement times normalized to, on the left, the H_{98} scaling law and on the right to the power degradation, $P^{-0.73}$, are plotted against n_{sep} .

The impact of n_{sep} on the confinement time normalized to the $H_{98y,2}$ scaling law in our L-mode database is very similar to the one reported in H-mode on AUG [10].

The fact that $H_{98y,2}$ values in the WEST L-mode database are similar to those in the AUG H-mode database reported in [10] is due to the unfavorable aspect ratio dependence of the $H_{98y,2}$ scaling law, while the L_{96} scaling law has a weak A dependence confirmed by WEST L-mode data [2]. This leads, at $A = 5$ – 6 , to similar confinement time prediction using the ITER96-L or the $H_{98y,2}$ scaling laws [1, 63].

The issue, when using the $H_{98y,2}$ scaling law for normalizing the confinement time, is that τ_{MHD} is normalized to $\bar{n}^{0.4}$, which is not what we observe in our database, see figure 4. Since \bar{n} and n_{sep} are correlated, see figure 1 below, keeping the unrealistic $\bar{n}^{0.4}$ scaling in the normalization of τ_{MHD} artificially exacerbates the detrimental impact of larger n_{sep} . To remove this bias, we normalize τ_{MHD} only to its power degradation. As expected, the destabilizing impact of n_{sep} is weaker, from $n_{sep}^{-0.23}$ for $T_e(0) > 2$ keV when using $H_{98y,2}$ down to $n_{sep}^{-0.12}$ with the power degradation normalization only. Nonetheless, the trend remains especially for $T_e(0) > 2$ keV.

4.3 Relation between density peaking and confinement time

We now compare the impact of \bar{n} , n_{sep} and the global density peaking $\bar{n}/\langle n \rangle$ on the normalized confinement to its power degradation $\tau_{MHD}/P^{-0.73}$, in figures 6(a)–(c), respectively. The correlation coefficient r is computed in each case across the whole database including all pulses, >2 keV and <2 keV. The clearest correlation of $\tau_{MHD}/P^{-0.73}$ is against the global density peaking, $r = 0.70$, while we report $r = -0.53$ with n_{sep} and a yet weaker correlation with \bar{n} , $r = -0.39$. Therefore, a more peaked density profile correlates both with larger $T_e(0)$ (figure 3(g)) and with better confinement time (figure 6(c)).

5. Role of the collisionality at the separatrix on confinement

As proposed in the 1990s by [18] and [15, 17, 64], resistive modes are likely to play near the separatrix of confined L-mode plasmas. These proposed theories were compared to experimental SOL data in L- and H-modes, see for example [19]. It actively continues today by comparing experimental trends to state-of-the-art edge simulations using gyrokinetic codes [20–23] and fluid nonlinear simulations [24–30]. Following the path of Scott and Rogers–Drake–Zeiler, fluid-based turbulent models are capturing qualitatively and quantitatively the density limit and/or the L–H transition [27, 28, 30, 31].

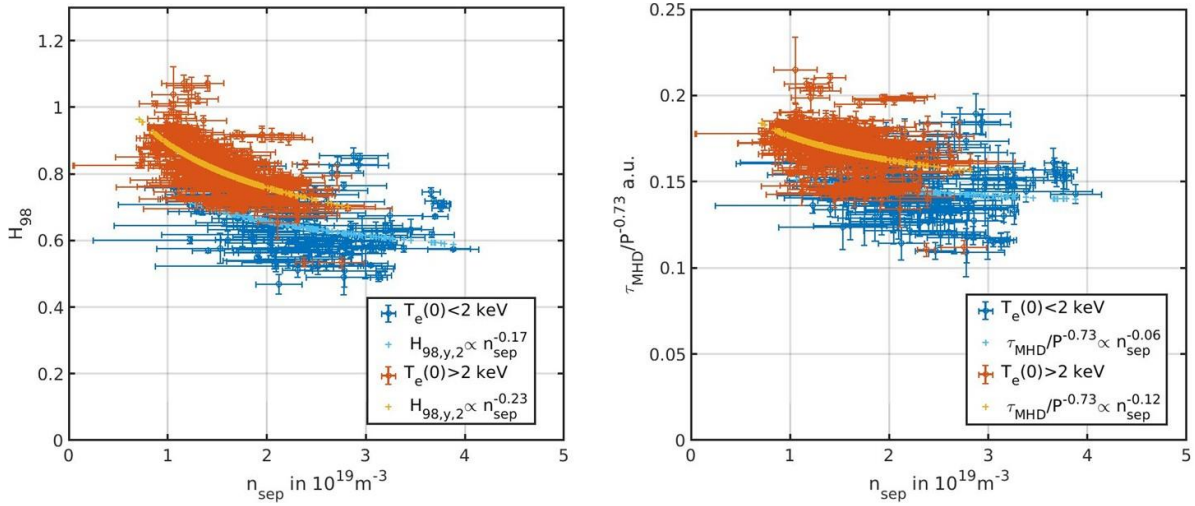


Figure 5. WEST C4–C5 L-mode database, $B = 3.7$ T, $I_p = 0.5$ MA, LSN, D only, $P_{tot} > 2$ MW. The confinement time is normalized to the $H_{98,y,2}$ scaling law on the left and to the power degradation, $P^{-0.73}$, on the right. The normalized τ_{MHD} is plotted versus the density at the separatrix measured by reflectometry, n_{sep} . The error bars represent the standard deviation measured during the plateaus over which the quantities are time averaged.

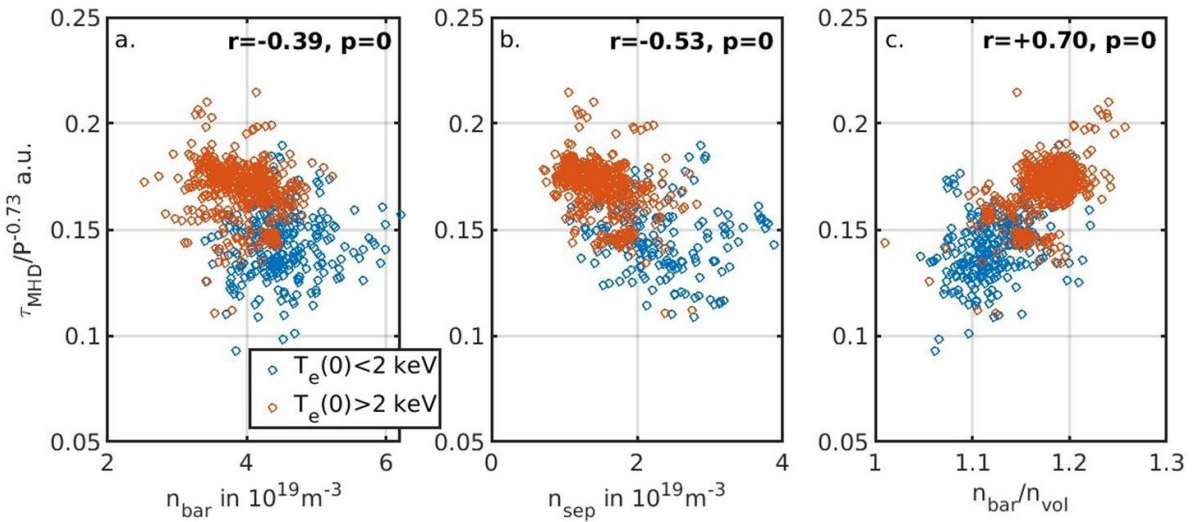


Figure 6. WEST C4–C5 L-mode database, $B = 3.7$ T, $I_p = 0.5$ MA, LSN, D only, $P_{tot} > 2$ MW. The confinement time is normalized to its power degradation and plotted against (a) the line-averaged density \bar{n} , (b) the density at the separatrix n_{sep} and (c) the density peaking global parameter $\bar{n}/\langle n \rangle$. r is the correlation coefficient and p is testing the hypothesis of a correlation, if $p < 0.05$ then the corresponding correlation is considered significant.

Hence, throughout the experimental database, one can expect to find some correlation between a normalized parameter characterizing the drive of resistive modes (typically scaling with the separatrix collisionality) and the overall plasma performances. Such a correlation is reported on AUG [11] where Thomson scattering allows estimation of the electron collisionality at the separatrix in both L- and H-modes. In JET, a Thomson scattering database in H-mode also shows that possibly resistive modes are at play when the pedestal confinement degrades before reaching the ideal MHD limit, at the highest densities [8].

On WEST, the Thomson scattering diagnostic allowing simultaneous measurement of the upstream density and temperature will be available from 2023 [65]. In the present

database, the density is measured by fast sweep reflectometry [56] around the separatrix. Concerning the temperature at the separatrix, the ECE signal is polluted by LHCD fast electrons for $\rho > 0.5$, and even in the absence of LHCD fast electrons, the optical depth when approaching the separatrix makes this measurement inappropriate in the separatrix region. On the other hand, on WEST, the downstream T_e and n_e on the divertor target are very well diagnosed by two arrays of 29 Langmuir probes covering the inner and outer divertor targets [66]. We have therefore applied the so called ‘two-point model’ on the parallel heat flux conservation to infer from the measured target T_t and parallel heat flux, $q_{\parallel,t}$, the upstream temperature, $T_{e,u} = T_{sep}$, as follows. From the energy conservation applied on the inner and outer divertor targets, one gets two equations

with two unknowns T_u and $L_{\parallel, \text{out}}$, the latter being the connection length from upstream to the outer target:

$$T_{e,u}^{7/2} = T_{e,t}^{7/2} + \frac{7}{2} \frac{1}{\kappa_{\parallel 0}} L_{\parallel, \text{out}} - L_{\parallel, \text{out}} q_{\parallel, \text{out}} f_{\text{cond}} f_{\text{in}} \quad (1)$$

$$T_{e,u}^{7/2} = T_{e,t}^{7/2} + \frac{7}{2} \frac{1}{\kappa_{\parallel 0}} L_{\parallel, \text{out}} q_{\parallel, \text{out}} f_{\text{cond}} f_{\text{out}} \quad (2)$$

where f_{cond} is the fraction of conducted power entering the SOL which is conducted towards the targets. f_{in} and f_{out} are the fractions conducted towards the inner and outer target, respectively.

Assuming $T_i = T_e$ along the flux tube from upstream to the target, one can replace the upstream parallel heat flux, $q_{\parallel, e, u}$, by the target fluxes on the inner and outer targets (respectively, $q_{\parallel, e, t, \text{in}}$ and $q_{\parallel, e, t, \text{out}}$) such that: $q_{\parallel, e, u} f_{\text{cond}} f_{\text{in}} = q_{\parallel, e, t, \text{in}} (1 - f_{\text{cooling, in}})$ and $q_{\parallel, e, u} f_{\text{cond}} f_{\text{out}} = q_{\parallel, e, t, \text{out}} (1 - f_{\text{cooling, out}})$. $f_{\text{cooling, in}}$ and $f_{\text{cooling, out}}$ are the fractions of the conducted power towards the inner and outer target, respectively, which are lost by radiation before reaching the target. $q_{\parallel, e, t} = \nu_e T_i j^+ / e$ is the

electron heat flux on target measured by the probes, using for the electron channel $\nu_e \approx 5$ as the sheath electron heat transmission coefficient. The inner and outer target quantities, $T_{e, t, \text{in}}$ and $T_{e, t, \text{out}}$ as well as $q_{\parallel, e, t, \text{in}}$ and $q_{\parallel, e, t, \text{out}}$, are respectively

taken as the maximum measured over the inner (resp. outer) target array made of 17 (resp. 12) Langmuir probes

The electron heat conductivity is $\kappa_{\parallel 0} \approx 2000/Z_{\text{eff}}$, with Z_{eff} the effective charge; here, we assume $Z_{\text{eff}} = 1$.

$L_{\parallel} = 2\pi R_{\text{geo}} q_{\text{cyl}}$ where the cylindrical q_{cyl} is defined as in [31].

As shown in [7], $(1 - f_{\text{cooling}}) \approx 1$ as long as $T_{e, t}$ is above 5 eV or so.

The strength of our estimate of T_{sep} is that, by using the probe measurements, we do not require assumptions on f_{cond} nor of the energy decay length λ_q .⁸ Assumptions are nonetheless made. In particular, we know that $T_i > T_e$ especially at low collisionality [67]. Indeed, T_i/T_e ratios larger than 1 are reported on various devices for example on the tokamaks Tore Supra [68], AUG [69] and the stellarator W7X [70]. Another parameter varying with target plasma parameter is the sheath electron transmission factor, see for example [71], here taken to be constant and equal to 5.

In this context, it is worth doing a simple consistency check using the second equation of the ‘two-point model’, the momentum conservation equation. The inferred upstream temperature, $T_{e, u} = T_{\text{sep}}$, should be such that:

$$n_{e, u} T_{e, u} f_{\text{mom}} = 2n_{e, t} T_{e, t} \quad (3)$$

assuming no dilution of the main ions and $T_i = T_e$ upstream and at the target plates, as assumed for the energy conservation.

$n_{e, t}$ is obtained from the Langmuir probes measurements as well [66]. $f_{\text{mom}} = (1 - f_{\text{mom, loss}})$, with $f_{\text{mom, loss}}$ is the

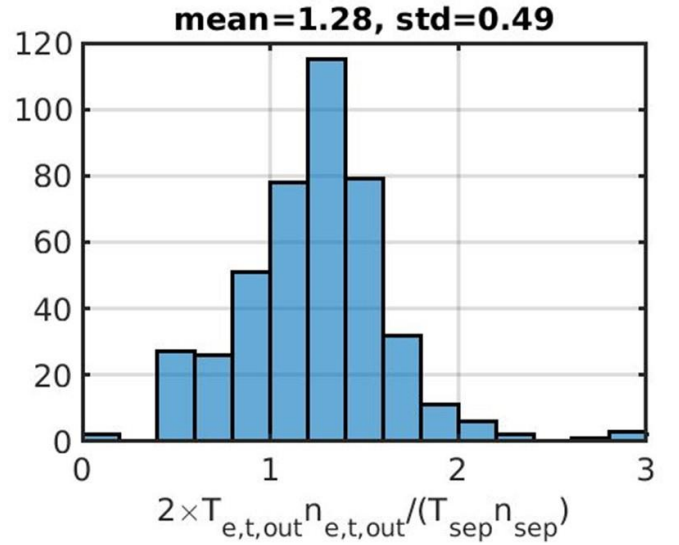


Figure 7. WEST C4–C5 database, $B = 3.7$ T, $I_p = 0.5$ MA, LSN, D

only, $P_{\text{tot}} > 2$ MW. Histogram of the ratio $\frac{2n_{e,t}T_{e,t}}{n_{e,u}T_{e,u}}$.

momentum loss factor. f_{mom} is expected to be around 1 for

$T_{e, t} > 3$ eV [7]. Therefore, if our estimate of $T_{e, u}$ is meaningful, $\frac{2n_{e,t}T_{e,t}}{n_{e,u}T_{e,u}} = f_{\text{mom}}$ is expected to vary over a reasonable range around 1. We observe in figure 7 below for all the plateaus that $\frac{2n_{e,t}T_{e,t}}{n_{e,u}T_{e,u}} = 1.28 \pm 0.49$. We therefore conclude that, although not exact, the two-point model energy conservation estimate of the electron temperature at the separatrix, $T_{e, u} = T_{\text{sep}}$, provides a reasonable estimate.

The validity of the two-point model is further discussed in appendix B where we compare the separatrix density and temperature with their target counterparts.

We now use the above estimate of $T_{e, \text{sep}}$ and obtain the operational domain $(n_{e, \text{sep}}, T_{e, \text{sep}})$ illustrated in figure 8. Surprisingly but very similarly to previously reported JET and CMod L- and H-modes database analysis in the conduction limited (high recycling) regime [72], WEST L-mode $T_{e, \text{sep}}$ is also proportional to $\sqrt{n_{\text{sep}}}$. In [72], $T_{e, \text{sep}} = c \sqrt{n_{\text{sep}}}$ with c ranging from 17 to 41 ($T_{e, \text{sep}}$ in eV and n_{sep} in 10^{19}m^{-3}) was reported for JET H- and L-modes in the gas box and MarkII divertors and Alcator C Mod H-modes. The third dimension in figure 8 is the SOL collisionality such that $10 \leq \nu_{\text{SOL}} \sim 10^{-16} \frac{L_{\parallel} n_{\text{sep}}}{T_{\text{sep}}} \leq 85$, confirming that WEST data is in the high recycling regime. Our best fit is $T_{e, \text{sep}} = 59.4 \sqrt{n_{\text{sep}}}$, see figure 8. More recently on JET-ITER-like wall (ILW) and Tokamak à Configuration Variable (TCV), in H-mode, the slight increase of $T_{e, \text{sep}}$ with larger n_{sep} has also been reported [73]. This observation is an interesting trend reported on various machines. Since in the present analysis $T_{e, \text{sep}} \propto \sqrt{n_{\text{sep}}}$ from the two-point model, the reported trend, $T_{\text{sep}} \propto \sqrt{n_{\text{sep}}}$, means that $n_{\text{sep}} \propto q_{\parallel, e, t}^4$.

⁸Note that in a separate work [85], a database of radial heat load profiles on the lower divertor targets measured by Langmuir probes, infrared thermography, thermocouples and fiber Bragg grating is presented and compared to an L-mode scaling law.

This means that in the high recycling cases considered here, higher density at the separatrix correlates with higher neutral particle fluxes on the target. The physics at play behind this correlation could be due to modified turbulent SOL transport and/or modified neutral recycled fluxes.

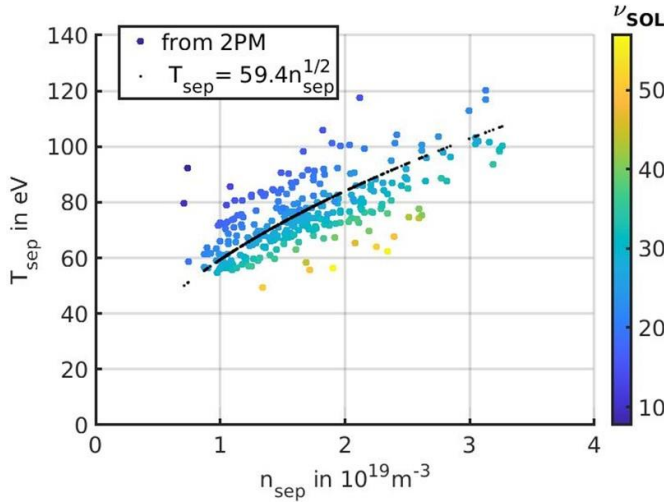


Figure 8. WEST C4–C5 database, $B = 3.7$ T, $I_p = 0.5$ MA, LSN, D only, $P_{\text{tot}} > 2$ MW. $T_{e,\text{sep}}$, obtained applying the two-point model (2PM) on target Langmuir probe measurement, is plotted against n_{sep} measured by reflectometry. The third dimension is the normalized collisionality at the separatrix: $\nu_{\text{sol}} \sim 10^{-16} \frac{L_{\parallel} n_{\text{sep}}}{T_{\text{sep}}^2}$.

A multi-machine database activity is being started including lower density cases to explore further such correlations. It is also an ideal challenge to be targeted by turbulent SOL-edge fluid codes, including neutral sources, such as SOLEDGE3X [74] and GRILLIX [75] for example.

In appendix C, the H-mode plateaus obtained in LSN are identified in the plane $(n_{e,\text{sep}}, T_{e,\text{sep}})$ where the formula proposed for the L–H transition and L-mode density limit frontiers in AUG [31] are traced as well. WEST data are compatible with these frontiers within the uncertainties on some quantities such as Z_{eff} and the characteristic perpendicular scale. For more details, the reader is referred to appendix C.

Using our two-point model estimate for $T_{e,\text{sep}}$ together with $n_{e,\text{sep}}$ measured by reflectometry, we can estimate the separatrix α_t parameter proposed in [11] such that $\alpha_t = 3.13 \times 10^{-18} R_{\text{geo}} Q^2 \frac{n_{\text{sep}}}{Z_{\text{eff}}} \cdot \alpha_t$ is the product of two parameters proposed in [17, 64]: a normalized collisionality C and a ratio between interchange and drift wave drive ω_b . α_t is similar to the parameter α_d proposed in [18]. The larger α_t is, the larger is the resistivity drive for turbulent transport.

While, in figure 5, we do report in WEST L-modes a confinement degradation with increased n_{sep} , similar to AUG and JET H-modes [10, 13], in figure 9, we do not observe a correlation of this confinement degradation with higher α_t unlike what has been reported on AUG H-modes [11]. This is due to the correlation, in our database, of larger T_{sep} with larger n_{sep} . Hence as n_{sep} increases, the normalized collisionality, embedded in α_t , or in ν_{sol} , does not increase as seen in figure 8, where we can see that an identical value of ν_{sol} can be obtained across the whole range of n_{sep} . Nonetheless, at a

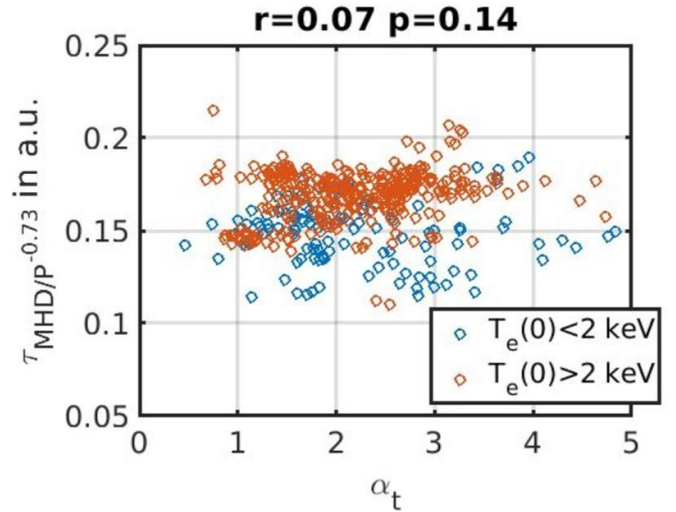


Figure 9. WEST C4–C5 database, $B = 3.7$ T, $I_p = 0.5$ MA, LSN, D only, $P_{\text{tot}} > 2$ MW. $\tau_{\text{MHD}}/P^{-0.73}$ is plotted against the normalized collisionality parameter $\alpha_t = 3.13 \times 10^{-18} R_{\text{geo}} Q^2 \frac{n_{\text{sep}}}{Z_{\text{eff}}} \cdot r$ is the correlation coefficient and p is testing the hypothesis of a correlation: if $p < 0.05$ then the corresponding correlation is considered significant.

factor of 5 variation of α_t is hence seen also along the x axis in figure 9.

This suggests that, in this L-mode database, the physics at play behind the confinement degradation with higher n_{sep} is not related to enhanced resistively driven turbulence.

In the following section, we will explore the role of neutrals on n_{sep} and possibly on the overall confinement.

6. Impact of fueled and recycled neutrals on density profile and confinement

Historically, the density at the separatrix has been presented as a control parameter at your fingertips, hypothesizing a link between n_{sep} and \bar{n} such that: $n_{\text{sep}} \sim 0.3\bar{n}$ [76]. Indeed, \bar{n} , the line-averaged central density measured by interferometry, is, given n_{sep} , ν_{sol} (or α_t) has a scatter factor ~ 5 on figure 8. This

in most if not all tokamaks, controlled in feedback by the gas puff rate (and/or pellet fueling) to match as best as possible the required waveform.

In our database, we find a weaker trend than the linear trend reported in the past $n_{sep} \sim 0.3\bar{n}$ [76]: $\bar{n} = 3.5 \times n^{0.3}$ with a large dispersion such that $\bar{n} = 4 \times 10^{19} \text{ m}^{-3}$ can be associated with n_{sep} between 1 and $4 \times 10^{19} \text{ m}^{-3}$, see figure 10.

Since gas fueling is used to control \bar{n} from the control room, and since \bar{n} weakly correlates with n_{sep} we do not expect n_{sep} to scale strongly with the gas puff. This is what is reported in figure 11(a). n_{sep} is plotted against the accumulated gas fueled in the vessel up to the plateau over which n_{sep} is time averaged. In contrast, in figure 11(b), n_{sep} correlates very strongly with the D recycled particle flux at the divertor inner and outer targets. The D flux is the maximum on each target of

sep
~ ~ x

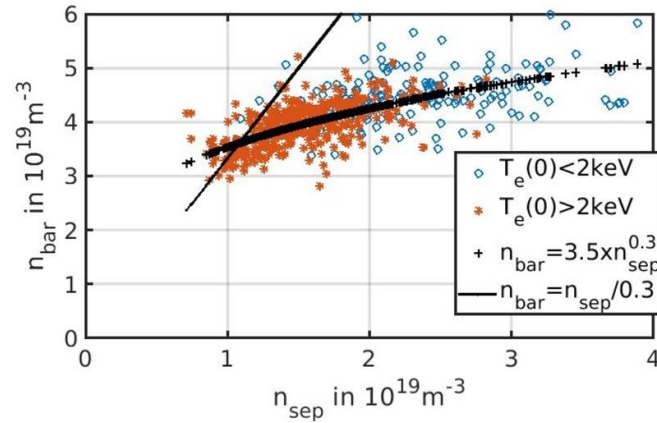


Figure 10. WEST C4–C5 L-mode database, $B = 3.7$ T, $I_p = 0.5$ MA, LSN, D only, $P_{\text{tot}} > 2$ MW. The plotted quantities are time averaged over the database plateaus. The line-averaged density from interferometry, n_{bar} , is plotted against the density at the separatrix, n_{sep} , measured by reflectometry. The plateaus over which the central electron temperature $T_e(0)$ is below 2 keV are in blue, and in red where $T_e(0) > 2$ keV.

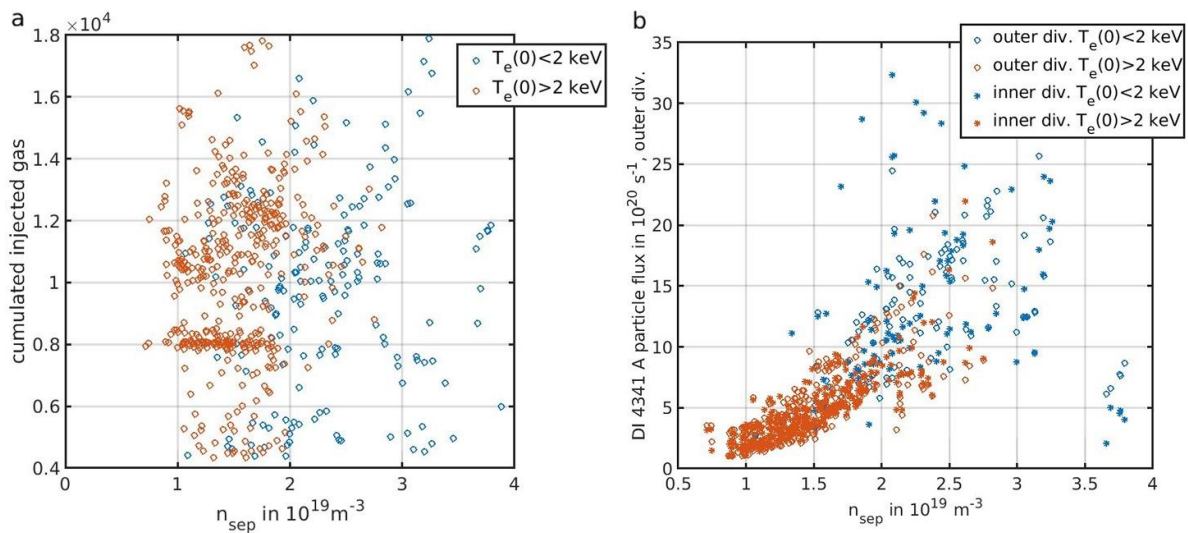


Figure 11. WEST C4–C5 L-mode database, $B = 3.7$ T, $I_p = 0.5$ MA, LSN, D only, $P_{\text{tot}} > 2$ MW. The plotted quantities are time averaged over the database plateaus. (a) Cumulated gas injected up to plateau initial time in mPa m^3 versus the density at the separatrix, n_{sep} , measured by reflectometry. (b) Neutral D flux from D_γ photon flux at 4341 \AA multiplied by S/XB against n_{sep} . The plateaus over which the central electron temperature $T_e(0)$ is below 2 keV are in blue, and in red where $T_e(0) > 2$ keV, the empty circles stand for the outer divertor (outer div.) and the full circles for the inner divertor (inner div.).

the D_γ emission (4341 \AA) measured by visible spectroscopy [77]. The neutral flux is obtained by multiplying the D_γ photon flux by the number of ionization events per photon, so-called S/XB. To obtain S/XB for $T_t > 20$ eV, we have interpolated between 1000 at $1 \times 10^{19} \text{ m}^{-3}$ and 5500 at $1 \times 10^{20} \text{ m}^{-3}$. A caveat remains, since these S/XB do not account for a potential photon source from D_2 molecular dissociation.

In appendix D, the similarity of the maximum of the photon fluxes on the inner and outer targets, observed in figure 11(b), are further discussed.

In the presence of neutral penetration, a lower n_{sep} is expected to allow neutrals being ionized deeper inside, leading to steeper electron density profile build-up inside the separatrix [32]. And indeed, using reflectometry data, we observe in figure 12(a) a strong correlation of larger density gradient

around the separatrix with lower n_{sep} . The opaqueness as defined in [34] is also reported to decrease for steeper density profiles, see appendix E for more details. This correlation of n_{sep} with its gradient is similar to the trend reported in JET H-modes [8].

Interestingly, similarly to the density peaking around the separatrix, the global density peaking from interferometry $\bar{n}/\langle n \rangle$ also anticorrelates with higher n_{sep} , although with a lower correlation factor, see figure 12(b).

As reported already for figure 3(g), more peaked density profiles correlate with hotter plasmas: this is recalled in figure 13(b). In figure 13(a), we observe also a strong correlation between more peaked density profiles and higher internal inductance. This is expected in LHCD-heated plasmas since the power deposition is more favorably absorbed centrally

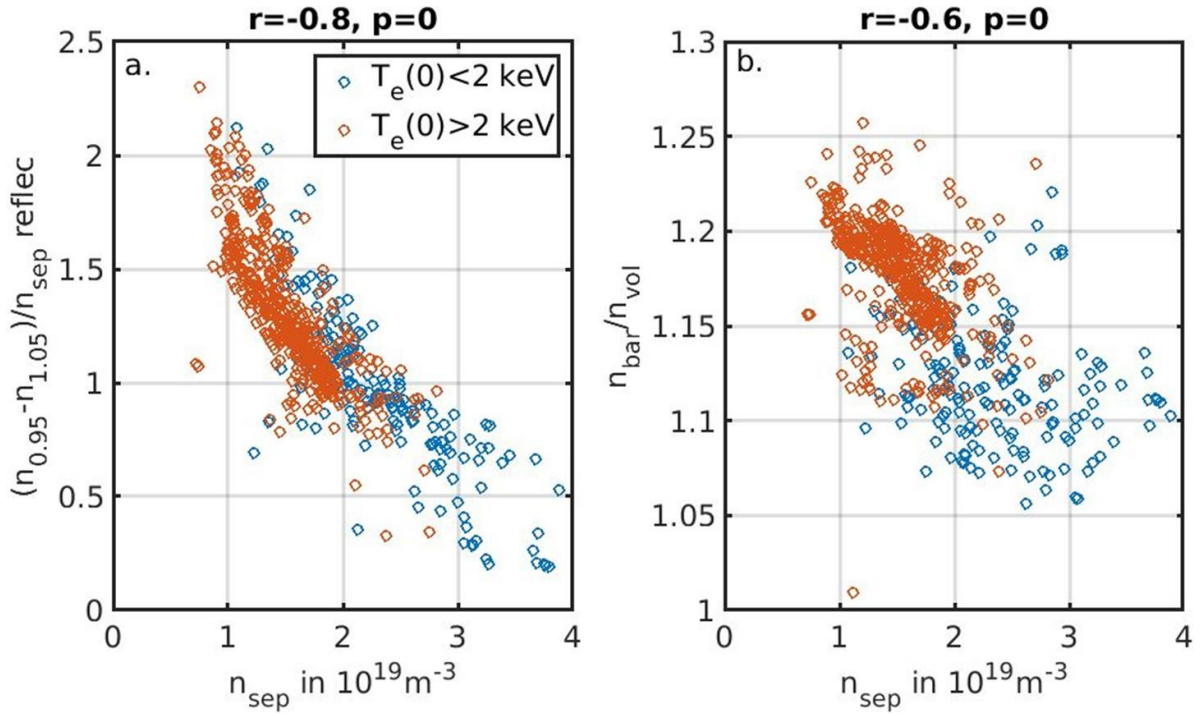


Figure 12. WEST C4–C5 L-mode database, $B = 3.7$ T, $I_p = 0.5$ MA, LSN, D only, reflectometry data, $P_{tot} > 2$ MW. The plotted quantities are time averaged over the database plateaus. (a) A proxy for the density peaking around the separatrix $(n_{0.95} - n_{1.05})/n_{sep}$ is plotted against n_{sep} , with $n_{0.95}$, n_{sep} and $n_{1.05}$ the density measured by reflectometry at the normalized poloidal magnetic flux of 0.95, at the separatrix and at the normalized poloidal magnetic flux of 1.05, respectively. (b) A proxy for the global density peaking given by the ratio of line-averaged to volume-averaged density, $\bar{n}/\langle n \rangle$ or n_{bar}/n_{vol} , provided by interferometry, is plotted against n_{sep} . The plateaus over which the central electron temperature $T_e(0)$ is below 2 keV are in blue, and in red where $T_e(0) > 2$ keV. r is the correlation coefficient and p is testing the hypothesis of a correlation: if $p < 0.05$ then the corresponding correlation is considered significant.

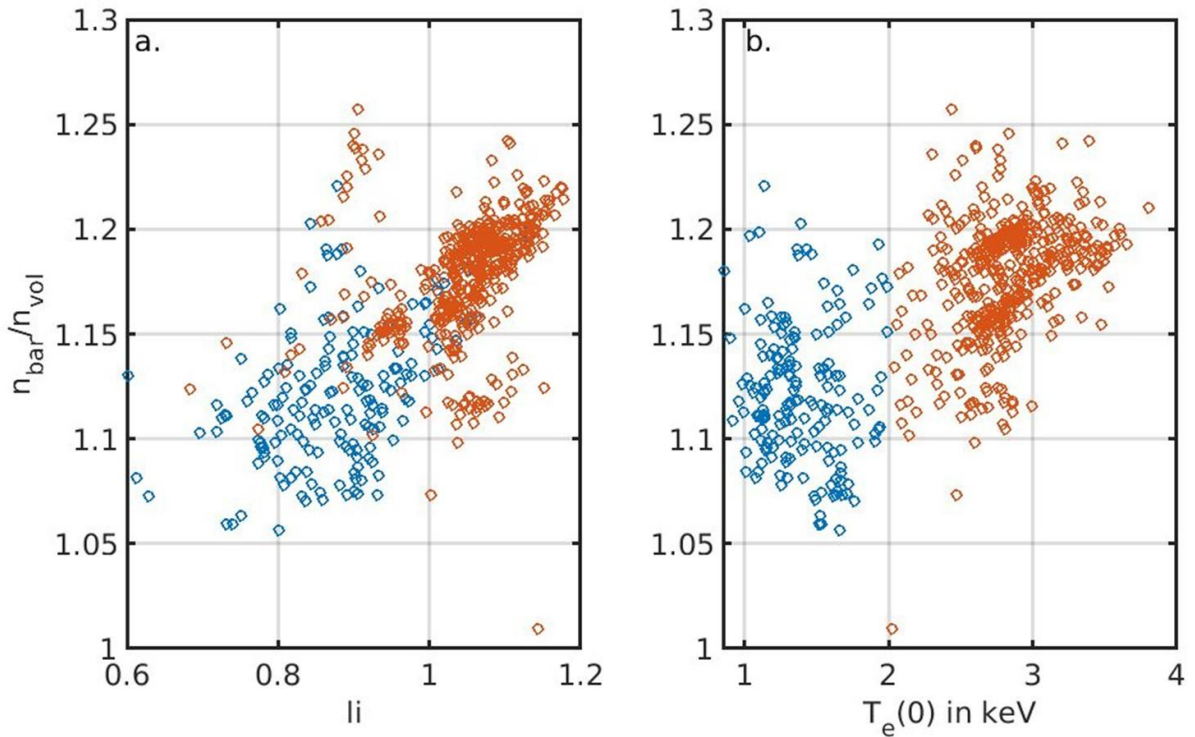


Figure 13. WEST C4–C5 L-mode database, $B = 3.7$ T, $I_p = 0.5$ MA, LSN, D only, $P_{tot} > 2$ MW. (a) A proxy for the global density peaking given by the ratio of line-averaged to volume-averaged density, $\bar{n}/\langle n \rangle$ or n_{bar}/n_{vol} , provided by interferometry, is plotted against the internal inductance li derived from the MHD equilibrium reconstruction constrained by polarimetry angles using NICE. (b) $\bar{n}/\langle n \rangle$ or n_{bar}/n_{vol} is plotted against the central electron temperature measured by ECE, $T_e(0)$. The plateaus over which the central electron temperature $T_e(0)$ is below 2 keV are in blue, and in red where $T_e(0) > 2$ keV.

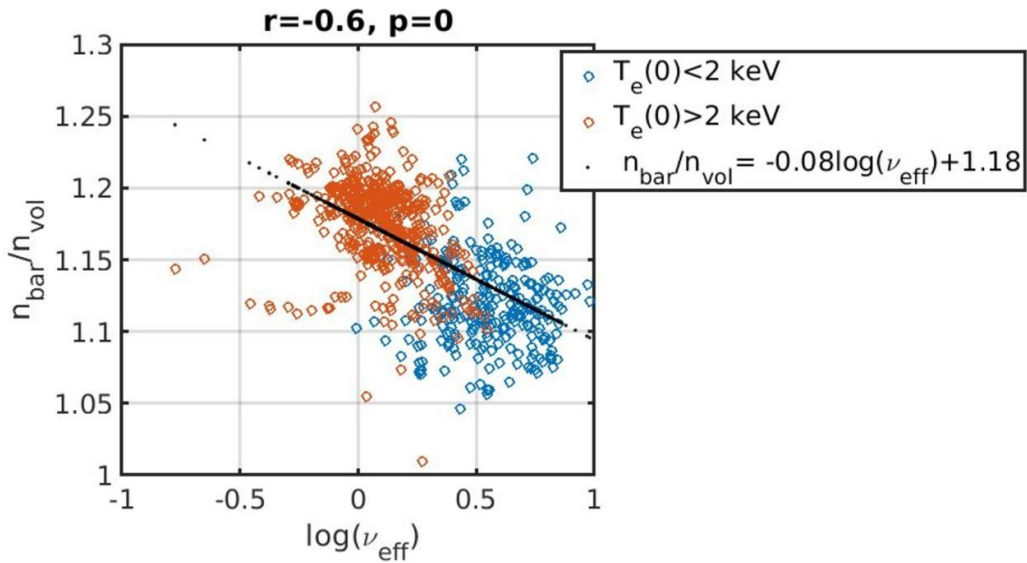


Figure 14. WEST C4–C5 L-mode database, LSN, $I_p = 0.5$ MA and $P_{tot} > 2$ MW. A proxy for the global density peaking given by the ratio of line-averaged to volume-averaged density, $\bar{n}/\langle n \rangle$ or n_{bar}/n_{vol} , provided by interferometry, is plotted against the log of a volume-averaged collisionality, ν_{eff} , as defined in [80]. The plateaus over which the central electron temperature $T_e(0)$ is below 2 keV are in blue, and in red where $T_e(0) > 2$ keV. r is the correlation coefficient and p is testing the hypothesis of a correlation: if $p < 0.05$ then the corresponding correlation is considered significant.

in hotter plasmas [51, 78]. We confirm the previously found scaling for the density peaking on the JET LHCD-heated L-mode database [79] such that $n_e(0)/\langle n \rangle \geq 1.6li$, see appendix F for more details.

The global density peaking was shown to correlate well with the volume-averaged effective collisionality $\nu_{eff} = 0.2 \frac{\langle n \rangle R_{geo}}{\langle T \rangle^2}$ [80]. We have therefore plotted $\bar{n}/\langle n \rangle$ over our database against ν_{eff} , see figure 14. We observe a correlation which is very similar to the previously reported correlation for RF-heated H-modes (equation (7) of [80]) such that

$$\frac{\bar{n}}{\langle n \rangle} = -0.08 \log(\nu_{eff}) + 1.18. \text{ We find a correlation coefficient}$$

$r = -0.6$. If we do the same exercise with respect to n_{sep} , figure 12(b), the correlation coefficient is identical, 0.6. Hence the question of the respective roles of core turbulent transport impacted by collisionality versus a potential impact of the density profile build-up around the separatrix on the plasma core is raised by the similar correlations reported here.

7. Conclusions and perspectives

L-mode, high recycling plasmas are an unavoidable phase of all plasma scenarios, during which performance optimization is mandatory to minimize the flux consumption, to ease H-mode access, to avoid MHD onset, etc.

The WEST L-mode database is analyzed from the SOL to the core. Quantities are averaged on identified plateaus at the intersection of stable power and plasma current lasting more than 0.3 s. The plasmas considered are in LSN and in D, at $I_p = 0.5$ MA with more than 2 MW of total power. Eight hundred plateaus populate the database, coming from pulses of the C4 and C5 campaigns (2019–2021) of WEST phase 1. Note that this database is automatically populated and made avail-

able to all WEST team members. Over these plateaus, parameters correlating with optimized core performances are searched for. By core performances we mean maximized core electron temperature at a given ratio of power to density and maximized energy content normalized to the power degradation $\tau_{MHD}/P^{-0.73}$ at a given (I_p, B_T) .

By definition, a database analysis cannot unveil the causality/ies. We can only report correlations and phrase the subsequent causality questions.

We have explored the correlations between core, separatrix and SOL quantities: the central electron temperature in

the core measured by ECE, $T_e(0)$; the global energy confinement quality $\tau_{MHD}/P^{-0.73}$; the global density peaking meas-

able to all WEST team members.

ured by interferometry, \bar{n}/n ; the separatrix density measured by reflectometry in the midplane mapped on a magnetic reconstruction constrained by magnetics and polarimetry, n_{sep} , as well as similar quantities at 0.95 and 1.05 normalized poloidal flux; the separatrix temperature inferred from the Langmuir probe parallel heat flux measured on the divertor targets using the so-called two-point model; the D particle flux at the divertor targets inferred from visible spectroscopy, etc.

We report correlations between a better energy confinement quality and a lower density at the separatrix (similar to AUG and JET H-modes [10, 13]) as well as with a larger global density peaking (figures 6(b) and (c)). The energy confinement quality does not correlate with the normalized collisionality at the separatrix (figure 9), unlike AUG H-modes [11]. The density at the separatrix, n_{sep} , is not a control parameter, in the sense that it does not correlate with the cumulated gas fueled in the vessel (figure 11(a)) nor with the feedback-controlled central line integrated density \bar{n} (figure 10). Rather we report that n_{sep} correlates with larger T_{sep} inferred from the two-point model (figure 8), hence, with larger parallel heat flux at the target. We also report that n_{sep} correlates with larger D neutral recycled fluxes on

()

the targets (figure 11(b)) and anticorrelates with the density gradient around the separatrix (figure 12(a)), as expected in a non-opaque plasma. The global density peaking, $\frac{n}{\langle n \rangle}$, is higher in hotter plasmas (figure 3(g) and 13) and correlates with larger internal inductance (figure 13(a)), while it anticorrelates with larger volume-averaged collisionality $v_{\text{eff}} \propto \frac{\langle n \rangle}{\langle T \rangle^2}$ (figure 14(a)). The global density peaking also anticorrelates with larger density at the separatrix (figure 14(b)).

These correlations pose the question of the causality chain between recycled neutrals at the targets, heat flux conducted to the target plates, density at the separatrix, density peaking around the separatrix and global peaking across the whole plasma, internal inductance, core temperature and overall energy confinement quality.

To summarize, WEST L-mode high recycling plasma database analysis allows formulating the following questions:

- What is the causality chain between low neutral recycling/low parallel heat flux on the divertor plates, low density at the separatrix, high density peaking at the separatrix, high global density peaking, higher central temperature and better L-mode core energy confinement?
- What are the consequences in terms of performance extrapolation towards larger machines (ITER and DEMO) where the neutral recycling and penetration through the separatrix will be different due to the smaller ratio of the ionization length to the divertor leg/wall clearance, weaker pumping efficiency with respect to the vacuum vessel volume, etc?

To answer these questions, the foreseen future work around the WEST plasma database is threefold:

- challenge the universality of the trends reported here in other tokamak L-mode databases such as the AUG L-mode database [31] and other tokamaks;
- explore the observed causality chain by integrating neutral penetration models with L-mode edge validated turbulent transport models across a significant subset of plateaus of the database using TGLF-sat2 [81] in the High Fidelity Pulse Simulator [82];
- in the event of successful integrated modeling, challenge the modeling suit on other divertor regimes and in other tokamaks, explore the consequences on future machine scenarios in ITER and DEMO.

Acknowledgments

The corresponding author would like to thank Bart Lomanowski, Thomas Eich and Y. Li as well as the EUROfusion TSVV11 team, in particular Clemente Angioni, for stimulating discussions.

This work has been carried out within the framework of the EUROfusion Consortium and has received funding from the European research and training program 2014-2018 and

2019-2020 under Grant Agreement No. 633053. The views and opinions expressed herein do not necessarily reflect those of the European Commission.

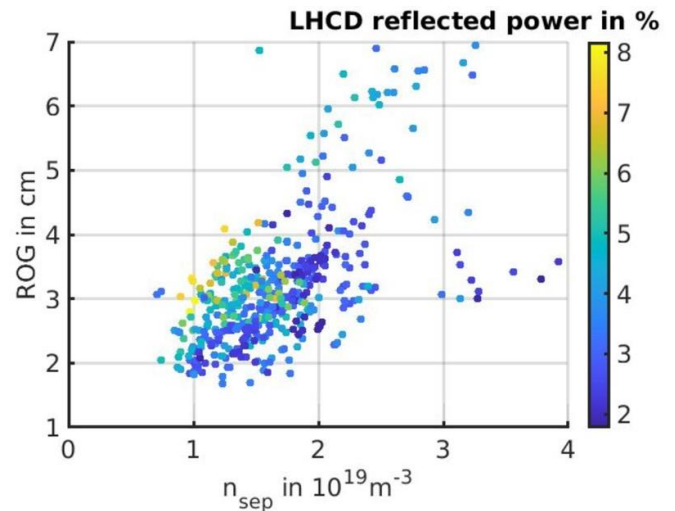


Figure 15. WEST C4–C5 L-mode database, $B = 3.7$ T, $I_p = 0.5$ MA, LSN, D only, $P_{\text{tot}} > 2$ MW. Color bar is the averaged LHCD reflected power in % (aveaged on the upper and lower rows of two LHCD launchers), time averaged over the plateaus.

Appendix A. LHCD coupling versus radial outer gap and n_{sep}

In the WEST L-mode database, the causality chain between the lower density at the separatrix and $T_c(0)$ could be the signature of a modified LHCD coupling. Indeed, in WEST, the three ICRH and two LHCD antennas are radially movable. For optimized LHCD, more fueling is required when the distance between the antenna and the confined plasma is larger [83]. This leads to an expected correlation between the density at the separatrix and the radial outer gap (or ROG, the gap between the plasma outboard midplane and the nearest among the five antennas). Over the LHCD-heated plateaus of the database we find a correlation parameter of $r = 0.5$ for $n_{\text{sep}} < 2 \times 10^{19} \text{ m}^{-3}$ which drops to $r = 0.1$ for $n_{\text{sep}} > 2 \times 10^{19} \text{ m}^{-3}$, see figure 15. At low n_{sep} , the ROG has to remain small (< 4 cm), while at higher n_{sep} higher ROG can be compatible with acceptable LHCD coupling. Overall, in the database, there is no one-to-one correlation between the LHCD coupling and n_{sep} and for all plateaus, the LHCD reflected power remains $< 8\%$, see figure 15.

Appendix B. Relation between the separatrix and target plasma quantities

In this appendix, we compare the separatrix quantities to the target ones and discuss the observations in light of the expectations from the two-point model.

The upstream density, n_{sep} , is predicted by the two-point model to scale, at fixed conducted power along the field lines, as $1/\sqrt{T_t}$ and $n_t^{1/3}$ [76]:

$$n_{\text{sep}} = 0.99 \Rightarrow \frac{mq_{\text{//u}}^{10/7} k_0^{4/7}}{v^2 T_t L^{4/7}}$$

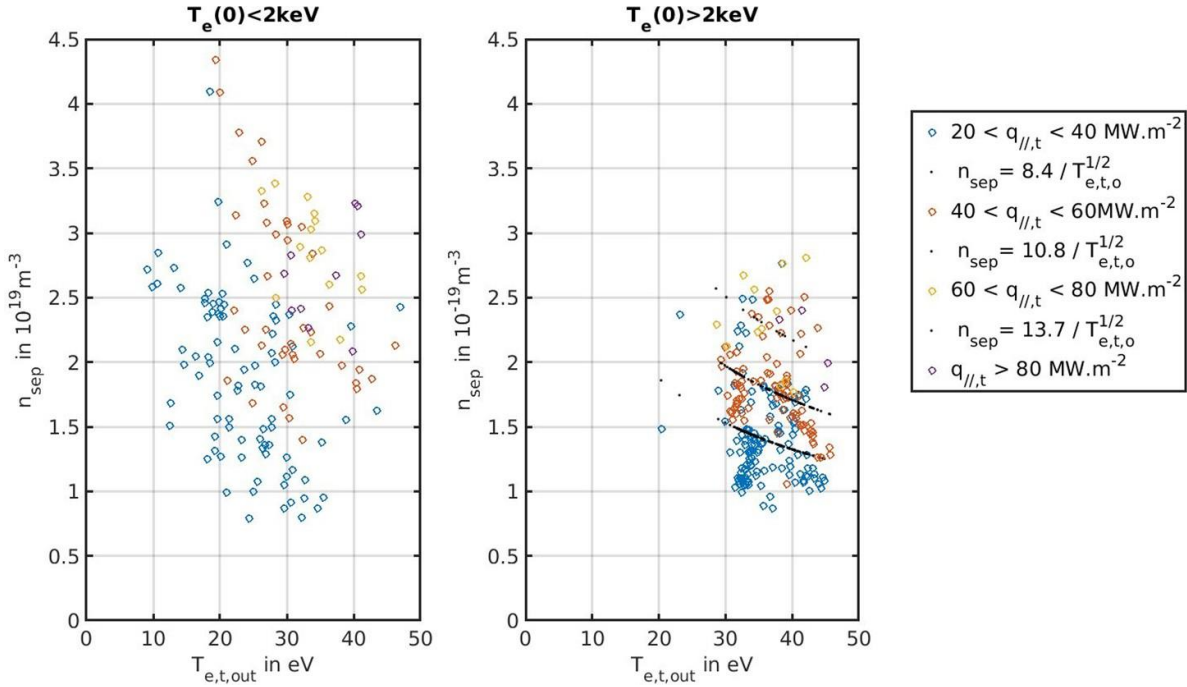


Figure 16. n_{sep} from reflectometry versus the maximum target temperature measured by Langmuir probes along the outer target, using plateau-averaged quantities on LSN pulses from the C4 campaign, in D, with more than 2 MW of total power and at 0.5 MA. On the left, pulses in which $T_e(0)$ is lower than 2 keV ‘cold branch’; on the right, $T_e(0) > 2$ keV ‘hot branch’. The maximum of the parallel heat flux on the outer target measured by Langmuir probes time averaged over the plateaus ($q_{||,t}$) is colored depending of its range: blue if ranging between 20 and 40 MW m⁻², yellow from 40 to 60 MW m⁻², red from 60 to 80 MW m⁻² and purple above 80 MW m⁻².

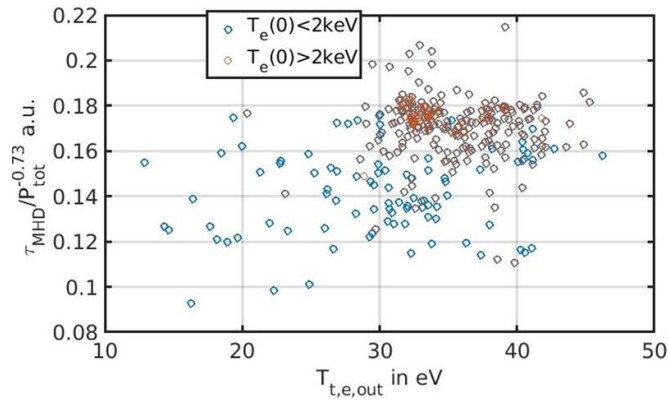


Figure 17. WEST C4 L-mode database, $B = 3.7$ T, $I_p = 0.5$ MA, LSN, D only, $P_{tot} > 2$ MW. The energy confinement time over its power degradation in arbitrary units: $\tau_{MHD}/P_{tot}^{-0.73}$ is plotted against the outer target temperature measured by Langmuir probes.

$$n_{sep} = 1.11 \frac{mq_{||,u} K_0 n_t}{\nu^2 L_{||}^{6/7}}$$

$$q_{||,u} = \frac{q_{||,e,t}}{f_{cond}}$$

In our database, a correlation of n_{sep} with $1/\sqrt{T_t}$ over a given range of $q_{||,t}$ is possibly found but only for $T_e(0)$ greater than 2 keV, see figure 16. Overall the range of T_t covered in our

database is too narrow to conclude on such a scaling, unlike in [7] where T varies from 2 to 40 eV.

In figure 16, for plateaus at $I_p = 0.5$ MA, $B_T = 3.7T$, we observe, on the cold branch ($T_e(0) < 2$ keV), that n_{sep} does not show any clear trend with respect to $T_{e,t,out}$ or $q_{||,t}$. On the hot branch, ($T_e(0) > 2$ keV), no correlation with $T_{e,t,out}$ is discernable, but we can see that the largest n_{sep} are indeed obtained for the largest $q_{||,t}$ and the converse.

We hence do not see a correlation between the core confinement and the temperature on the target, see figure 17, unlike on JET [7]. This is not inconsistent with [7] where the trend

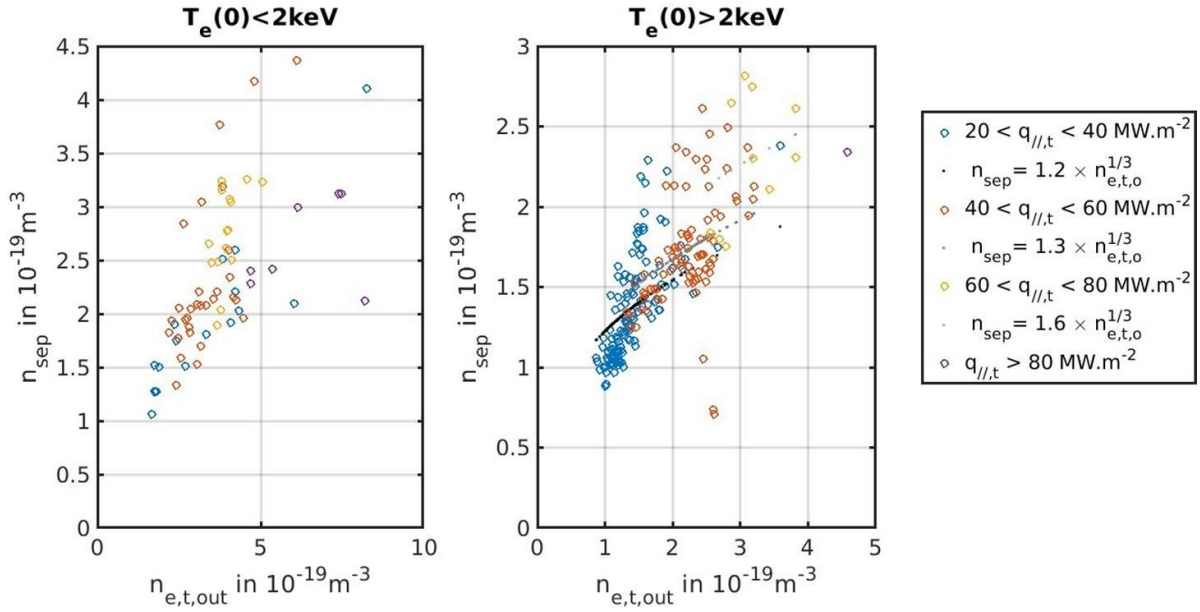


Figure 18. n_{sep} from reflectometry versus the maximum target density measured by Langmuir probes along the outer target. Plateau averaged quantities on LSN pulses from the C4 campaign, in D, with more than 2 MW of total power and at 0.5 MA. On the left pulses in which $T_e(0)$ is lower than 2 keV ‘cold branch’, on the right where $T_e(0) > 2$ keV ‘hot branch’. The maximum of the parallel heat flux on the outer target measured by LP time averaged over the plateaus ($q_{\parallel,t}$) is colored depending of its range: blue if ranging between 20 and 40 MW m⁻², yellow from 40 to 60, red from 60 to 80 and purple above 80 MW m⁻².

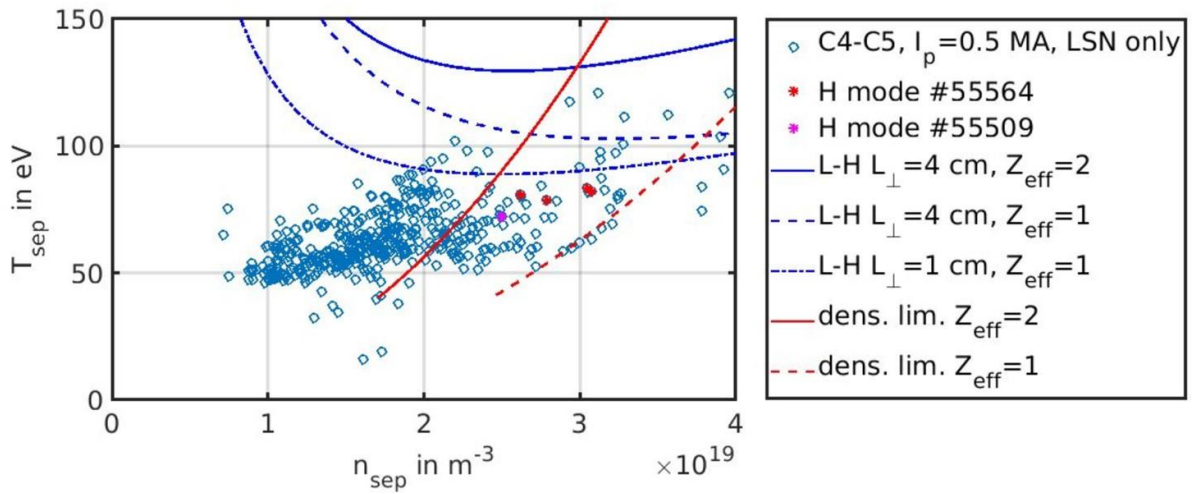


Figure 19. Separatrix operational space of WEST in terms of electron density and temperature. The red line shows the boundary of the L-mode density limit (equation (3) of [31]). The blue line indicates the L–H–L transition (equation (8) of [31]). The impact of L_{\perp} and Z_{eff} are tested: full versus dashed and dot-dashed lines. The H-mode phases are highlighted in red and magenta.

of the confinement with respect to $T_{e,t,\text{out}}$ is mostly reported in H-modes and for $T_{e,t,\text{out}} \leq 10$ eV.

Concerning the correlation between n_{sep} and the maximum density measured by Langmuir probes along the outer divertor target, we do not find the expected trend from the two-point model $n_{\text{sep}} \propto n_t^{1/3}$ over the database. We rather observe a larger scatter of achieved n_{sep} at a given n_t as reported in figure 18. Nonetheless, the minimum accessible n_{sep} seems to increase as $n_t^{1/3}$, especially for the subset of data such that $T_e > 2$ keV.

Appendix C. Separatrix operational space versus predicted L–H and density limit frontiers proposed on AUG

The separatrix operational space of WEST in terms of electron density and temperature is tested against the H-mode access and density limit frontiers proposed in [31].

The database plotted in figure 8 is replotted below in figure 19, and the plateaus identified as being in H-mode are

highlighted in red and magenta. Only the H-mode plateaus in LSN and such that both reflectometry and Langmuir probes data are available appear here (more details on H-mode phases in WEST phase 1 in [3]).

A perpendicular gradient length and an effective charge are needed in equations (3) and (8) of [31] to determine the L-mode density limit and the L–H–L transition, respectively. In the absence of pressure gradient length information in our database (no Thomson scattering), we use the density gradient length as a proxy for a reference perpendicular gradient length L_{\perp} . $L_{\perp} = 4$ cm is the density gradient length from reflectometry averaged over the C4–C5 LSN database analyzed here. $Z_{\text{eff}} = 2$ is the mean resistive Z_{eff} of the database. With these values, we find the full lines in figure 19, in blue for the L–H transition and in red for the density limit.

With $Z_{\text{eff}} = 2$, the density limit is not consistent with our database: it predicts a too low density limit. By reducing Z_{eff} down to 1, hence, the drive for resistive modes, the density limit frontier becomes coherent with our database. Reducing Z_{eff} also reduces the predicted frontier between L- and H-mode. Reducing L_{\perp} as well as Z_{eff} lowers further the L–H transition frontier and it becomes closer to the observed transitions. At this stage, the inconsistencies are difficult to discuss further as uncertainties on T_{sep} are large (assumed from

the two-point model applied on Langmuir probe target data assuming no equipartition) as well as the uncertainties on the pressure gradient length, here approximated by the reflectometry density gradient length averaged over the database. Despite the limitation of the present data set, it is interesting to see that the proposed physics mechanisms for H-mode access and density limit consistent with AUG database [31] could also be consistent with WEST data. This will be revisited when more H-mode phases will have been collected and when the Thomson scattering diagnostic is in operation.

Appendix D. Symmetry on inner and outer targets of energy and particle fluxes

As reported in figure 11(b), the maximum of the D γ photon flux over the inner and outer targets are remarkably similar, and is confirmed below in figure 20(a) for fluxes $< 10^{18}$ s $^{-1}$, while above 10^{18} s $^{-1}$ the fluxes on the inner target become larger as also reported for O $^{3+}$ emission along the targets [84]. The parallel heat flux on the targets is, as expected, larger on the outer target [85], with about two times more heat flux on the outer target than on the inner, figure 20(b). Above 50 MW m $^{-2}$ the inner target parallel heat flux values increase much faster than the outer ones.

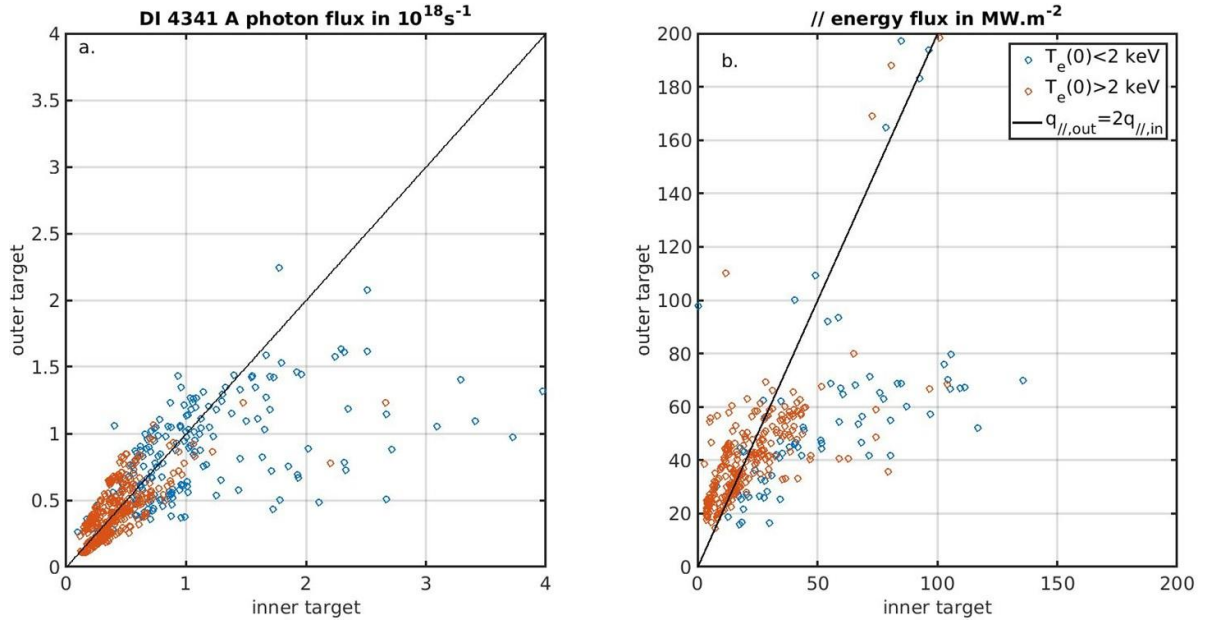


Figure 20. WEST C4–C5 L-mode database, $B = 3.7$ T, $I_p = 0.5$ MA, LSN, D only, $P_{tot} > 2$ MW. (a) shows the $D\gamma$ photon flux: inner vs outer targets. (b) show the parallel heat flux on the outer target against the inner target flux.

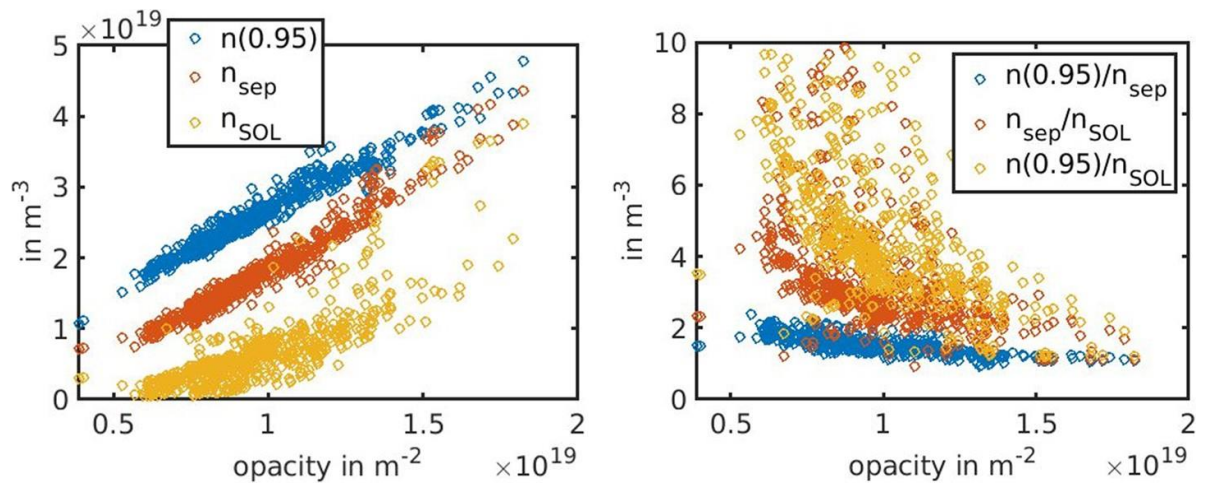


Figure 21. WEST C4–C5 L-mode database, $B = 3.7$ T, $I_p = 0.5$ MA, LSN, D only, $P_{tot} > 2$ MW. The densities are measured by reflectometry at 0.95, 1 and 1.05 of normalized poloidal flux for $n(0.95)$, n_{sep} and n_{SOL} , respectively.

Appendix E. Opaqueness in the WEST L-mode database

In [34], the opaqueness is defined such that, for a given toroidal device, it is proportional to $n \times a$, assuming that the boundary region thickness is proportional to minor radius a and approximating the density inside the separatrix by $n = \frac{n_{e,ped} + n_{e,sep}}{2}$. In our L-mode cases we use: $n = \frac{n_{e(0.95)} + n_{e,sep}}{2}$. As illustrated in figure 21, the range of opaqueness we cover is similar to

DIII-D for example, while on ITER ten times higher opaqueness is expected [34]. We plot figures similar to figure 15 of [34] on DIII-D and Alcator C-Mod, and unlike these DIII-D and Alcator C-Mod H-mode cases at higher opaqueness (ranging from 2 to 5 10^{19} m^{-2}), here the density profile steep-ening decreases as the opaqueness increases, as expected for cases where the neutral penetration plays a role. In figure 21, n_{SOL} is the density given by reflectometry at 1.05 of normalized poloidal flux.

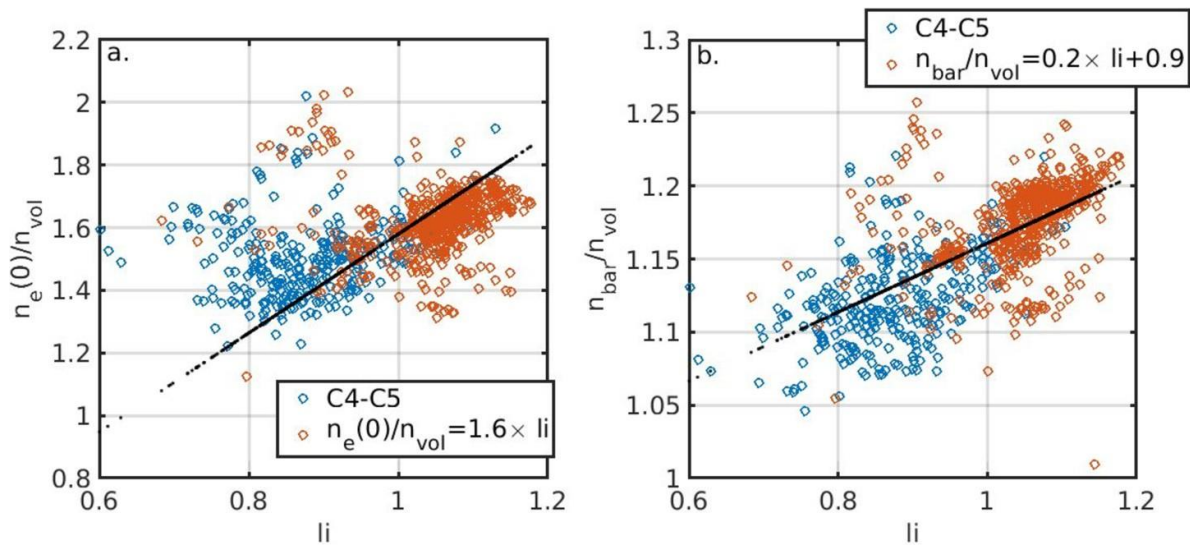


Figure 22. WEST C4–C5 L-mode database, $B = 3.7$ T, $I_p = 0.5$ MA, LSN, D only, $P_{tot} > 2$ MW.

Appendix F. Global density peaking versus internal inductance

A strong correlation between the global density peaking and the internal inductance has been reported in the past [79] on an L-mode JET database with LHCD heating such that: $n_e(0) / \bar{n} \geq 1.6xli$ (figure 7 of [79]). And in our data-base we find the exact same regression $n_e(0) / \bar{n} \geq 1.6xli$ (figure 22(a)). Note that, in figure 22(b), we observe less scatter by plotting rather n_{bar}/n_{vol} against the internal inductance. Since better confinement correlates with higher $T_e(0)$ and higher $T_e(0)$ with more centrally deposited LHCD, as in JET L-mode cases, we do expect in our database a strong correlation between larger li and hotter core. So we cannot disentangle the possible roles of core collisionality and core current profile peaking on the overall density peaking.

ORCID iDs

C. Bourdelle · <https://orcid.org/0000-0002-4096-8978>

R. Dumont · <https://orcid.org/0000-0002-1030-138XJ>

Gaspar · <https://orcid.org/0000-0003-0104-1616>

P. Maget · <https://orcid.org/0000-0002-8746-8102>

References

- [1] Bucalossi J. et al 2022 *Nucl. Fusion* **62** 042007
- [2] Goniche M. et al 2022 *Nucl. Fusion* **62** 126058
- [3] Vermare L. et al 2022 *Nucl. Fusion* **62** 026002
- [4] Martin Y.R. et al 2008 *J. Phys.: Conf. Ser.* **123** 012033
- [5] Imbeaux F. et al 2015 *Nucl. Fusion* **55** 123006
- [6] Ostuni V. et al 2022 *Nucl. Fusion* **62** 106034
- [7] Lomanowski B. et al 2022 *Nucl. Fusion* **62** 066030
- [8] Frassinetti L. et al 2021 *Nucl. Fusion* **61** 126054
- [9] Maslov M., Boboc A., Brix M., Flanagan J.C., Peluso E., Price C. and Romanelli M. 2020 *Nucl. Fusion* **60** 036007
- [10] Ryter F. et al 2021 *Nucl. Fusion* **61** 046030
- [11] Eich T., Manz P., Goldston R.J., Hennequin P., David P., Faitsch M., Kurzan B., Sieglin B. and Wolfrum E. 2020 *Nucl. Fusion* **60** 056016
- [12] Luda T., Angioni C., Dunne M.G., Fable E., Kallenbach A., Bonanomi N., Schneider P.A., Siccino M. and Tardini G. 2020 *Nucl. Fusion* **60** 036023
- [13] Verdoolaege G. et al 2021 *Nucl. Fusion* **61** 076006
- [14] Porter G.D. et al 1999 *J. Nucl. Mater.* **266–269** 917–21
- [15] Scott B. 1997 *Plasma Phys. Control. Fusion* **39** 1635
- [16] Scott B.D. 2003 *Plasma Phys. Control. Fusion* **45** A385
- [17] Scott B.D. 2005 *Phys. Plasmas* **12** 062314
- [18] Rogers B.N., Drake J.F. and Zeiler A. 1998 *Phys. Rev. Lett.* **81** 4396
- [19] LaBombard B., Hughes J.W., Mossessian D., Greenwald M., Lipschultz B., Terry J.L. and Team T.A.C.-M. 2005 *Nucl. Fusion* **45** 1658
- [20] Bourdelle C., Garbet X., Singh R. and Schmitz L. 2012 *Plasma Phys. Control. Fusion* **54** 115003
- [21] Bourdelle C. et al 2014 *Nucl. Fusion* **54** 022001
- [22] Bonanomi N., Angioni C., Crandall P.C., Di Siena A., Maggi C.F. and Schneider P.A. 2019 *Nucl. Fusion* **59** 126025
- [23] Bonanomi N., Angioni C., Plank U., Schneider P.A. and Maggi C.F. 2021 *Phys. Plasmas* **28** 052504
- [24] Zhu B., Francisquez M. and Rogers B.N. 2017 *Phys. Plasmas* **24** 055903
- [25] Hajjar R.J., Diamond P.H. and Malkov M.A. 2018 *Phys. Plasmas* **25** 062306
- [26] Stegmeir A. et al 2019 *Phys. Plasmas* **26** 052517
- [27] De Dominicis G., Fuhr G., Bourdelle C., Beyer P., Garbet X., Sarazin Y. and Falchetto G.L. 2019 *Nucl. Fusion* **59** 126019
- [28] Giacomini M. and Ricci P. 2020 *J. Plasma Phys.* **86** 905860502
- [29] Tatali R., Serre E., Tamain P., Galassi D., Ghendrih P., Nespoli F., Bufferand H., Cartier-Michaud T. and Ciraolo G. 2021 *Nucl. Fusion* **61** 056002
- [30] Giacomini M., Pau A., Ricci P., Sauter O. and Eich T. (the ASDEX Upgrade Team, JET Contributors, and the TCX Team) 2022 *Phys. Rev. Lett.* **128** 185003
- [31] Eich T., Manz P. (the ASDEX Upgrade Team) 2021 *Nucl. Fusion* **61** 086017
- [32] Groebner R.J., Mahdavi M.A., Leonard A.W., Osborne T.H., Porter G.D., Colchin R.J. and Owen L.W. 2002 *Phys. Plasmas* **9** 2134

- [33] Saarelma S., Challis C.D., Garzotti L., Frassinetti L., Maggi C.F., Romanelli M. and Stokes C. 2018 *Plasma Phys. Control. Fusion* **60** 014042
- [34] Mordijck S. 2020 *Nucl. Fusion* **60** 082006
- [35] Tsui C.K. *et al* 2022 *Phys. Plasmas* **29** 062507
- [36] Stotler D.P., Lang J., Chang C.S., Churchill R.M. and Ku S. 2017 *Nucl. Fusion* **57** 086028
- [37] Boyle D.P., Majeski R., Schmitt J., Hansen C., Kaita R., Kubota S., Lucia M. and Rognlén T. 2017 *Phys. Rev. Lett.* **119** 015001
- [38] Mukhovatov V. *et al* 2003 *Plasma Phys. Control. Fusion* **45** A235
- [39] Wenninger R. *et al* 2017 *Nucl. Fusion* **57** 016011
- [40] Xie H., Chan V.S., Ding R., Shi N., Jian X., Zagórski R., Ivanova-Stanik I., Chen J., Chen J. and Li J. 2020 *Nucl. Fusion* **60** 046022
- [41] Pitts R.A. *et al* 2019 *Nucl. Mater. Energy* **20** 100696
- [42] Day C. *et al* 2022 *Fusion Eng. Des.* **179** 113139
- [43] Bourdelle C. 2020 *Nucl. Fusion* **60** 102002
- [44] Schuster C.U. *et al* 2022 *Nucl. Fusion* **62** 066035
- [45] Tala T. *et al* 2019 *Nucl. Fusion* **59** 126030
- [46] Unterberg B., Samm U., Tokar' M.Z., Messiaen A.M., Ongena J. and Jaspers R. 2005 *Fusion Sci. Technol.* **47** 187–201
- [47] Tokar M.Z., Ongena J., Unterberg B. and Weynants R.R. 2000 *Phys. Rev. Lett.* **84** 895
- [48] Faugeras B. and Orsitto F. 2018 *Nucl. Fusion* **58** 106032
- [49] Faugeras B. 2020 *Fusion Eng. Des.* **160** 112020
- [50] Tsitroni E. *et al* 2022 *Nucl. Fusion* **62** 076028
- [51] Dumont R., Giruzzi G. and Barbato E. 2000 *Phys. Plasmas* **7** 4972
- [52] Nilsson E. *et al* 2013 *Nucl. Fusion* **53** 083018
- [53] Devynck P., Fedorczak N., Mao R. and Vartanian S. 2021 *J. Phys. Commun.* **5** 095008
- [54] Hillairet J. *et al* 2021 *Nucl. Fusion* **61** 096030
- [55] Gil C., Colledani G., Domenes M., Volpe D., Berne A., Faisse F., Guillon C., Morales J., Moreau P. and Santraine B. 2019 *Fusion Eng. Des.* **140** 81–91
- [56] Clairet F., Bottereau C., Medvedeva A., Molina D., Conway G.D., Silva A. and Stroth U. 2017 *Rev. Sci. Instrum.* **88** 113506
- [57] Morales J. *et al* 2022 Operational space for Lower Hybrid scenarios in the full tungsten environment of WEST 64th Annual Meeting of the APS Division of Plasma Physics (Spokane, Washington, 17–21 October 2022) (Bulletin of the American Physical Society) (available at: <https://hal-cea.archives-ouvertes.fr/cea-03863834/>)
- [58] Kaye S.M., Demanins R. and Bex P.J. 1997 *Nucl. Fusion* **37** 1303
- [59] Shimomura Y., Aymar R., Chuyanov V., Huguet M. and Parker R. (ITER Joint Central Team) 1999 *Nucl. Fusion* **39** 1295
- [60] Yushmanov P.N., Takizuka T., Riedel K.S., Kardaun O.J.W.F., Cordey J.G., Kaye S.M. and Post D.E. 1990 *Nucl. Fusion* **30** 1999
- [61] Ostuni V. 2022 Impact of plasma composition and aspect ratio on overall tokamak performance *PhD defense* Aix-Marseille Université, France *Physique et Sciences de la Matière* (available at: <https://hal-cea.archives-ouvertes.fr/tel-03879621/>)
- [62] Peysson Y. 1993 *Plasma Phys. Control. Fusion* **35** B253
- [63] Bourdelle C. *et al* 2019 46th European Physical Society Conf. on Plasma Physics (Milan, Italy, 8–12 July 2019) (available at: https://pure.mpg.de/rest/items/item_3168802/component/file_3317730/content)
- [64] Scott B.D. 2007 *Plasma Phys. Control. Fusion* **49** S25
- [65] Chelih B., Colledani G., Doceul L., Lefèvre N., Batal T., Garitta S., Faisse F., Verger J.-M. and Bec A. 2022 *Appl. Sci.* **12** 1318
- [66] Dejarnac R., Sestak D., Gunn J.P., Firdaouss M., Greuner H., Pascal J.-Y., Richou M. and Roche H. 2021 *Fusion Eng. Des.* **163** 112120
- [67] Stangeby P.C. 2000 The plasma boundary of magnetic fusion devices (Bristol: Institute of Physics Publishing) (available at: <http://data.lib.hutchedu.vn/mucluc/d456afd00c0e17e699ebb904ac38de19.pdf>)
- [68] Kocan M. *et al* 2009 *J. Nucl. Mater.* **390–391** 1074–7
- [69] Reich M., Wolfrum E., Schweinzer J., Ehmler H., Horton L.D. and Neuhauser J. (ASDEX Upgrade Team) 2004 *Plasma Phys. Control. Fusion* **46** 797
- [70] Li Y. *et al* 2019 *Nucl. Fusion* **59** 126002
- [71] Mijin S., Militello F., Newton S., Omotani J. and Kingham R.J. 2020 *Plasma Phys. Control. Fusion* **62** 125009
- [72] Ereñts S.K., Stangeby P.C., LaBombard B., Elder J.D. and Fundamenski W. 2000 *Nucl. Fusion* **40** 295
- [73] Balbin-Arias J.J., Bucalossi J., Bufferand H. and Ciraolo G. 2020 *Contrib. Plasma Phys.* **60** 5–6
- [74] Bufferand H. *et al* 2021 *Nucl. Fusion* **61** 116052
- [75] Stegmeir A., Coster D., Ross A., Maj O., Lackner K. and Poli E. 2018 *Plasma Phys. Control. Fusion* **60** 035005
- [76] Pitcher C.S. and Stangeby P.C. 1997 *Plasma Phys. Control. Fusion* **39** 779
- [77] Meyer O., Tulej M. and Wurz P. 2018 *Rev. Sci. Instrum.* **89** 10
- [78] Peysson Y. and Decker J. 2014 *Fusion Sci. Technol.* **65** 22–42
- [79] Weisen H. *et al* 2005 *Nucl. Fusion* **45** L1
- [80] Angioni C. *et al* 2007 *Nucl. Fusion* **47** 1326
- [81] Angioni C., Gamot T., Tardini G., Fable E., Luda T., Bonanomi N., Kiefer C.K. and Staebler G.M. (ASDEX Upgrade Team, EUROfusion MST1 Team) 2022 *Nucl. Fusion* **62** 066015
- [82] Bourdelle C. *et al* 2022 *Bulletin of the American Physical Society 64th Annual Meeting of the APS Division of Plasma Physics (Spokane, Washington, 17–21 October 2022)* (available at: <https://meetings.aps.org/Meeting/DPP22/Session/YP11.1>)
- [83] Delpéch L. *et al* 2020 *AIP Conf. Proc.* **2254** 080004
- [84] Gallo A. *et al* 2020 *Nucl. Fusion* **60** 126048
- [85] Gaspar J. *et al* 2021 *Nucl. Fusion* **61** 096027
- [86] Saibene G. *et al* 2002 *Plasma Phys. Control. Fusion* **44** 1769